

20

25



A Dimensionless-Entropy Weight Method for Determining Cloud Physical Parameter Responses Induced by Aircraft Cloud Seeding

Xiuzhu Sha^{1,2} Xingyu Li^{3,*} Jianfang Ding^{1,2} Ronghao Chu^{1,4} Bo Cheng^{1,2} Yanhua Liu^{1,2} Fan Zhang^{1,2} Can Song^{1,2} Yao Xiao^{1,5} Shanhai Wang^{1,2}

¹China Meteorological Administration•Henan Key Laboratory of Agrometeorological Support and Applied Technique, Zhengzhou 450003, China

²Weather Modification Center of Henan Province, Zhengzhou 450003, China

³Institute of Atmospheric Physics, Chinese Academy of Sciences, Beijing 100029, China

⁴Henan Institute of Meteorological Sciences, Zhengzhou 450003, China

⁵Meteorological Service Center of Henan Province, Zhengzhou 450003, China

Correspondence to: Xingyu Li (lxy@mail.iap.ac.cn), Ronghao Chu (ronghao_chu@163.com).

Abstract: To address the challenges in evaluation of aircraft cloud seeding effect, this study proposes a physical evaluation method that integrates multiple key techniques to achieve an integrated quantitative evaluation based on multiple indicators. This evaluation approach was applied to six aircraft cloud seeding operations conducted in Henan Province of China during 2023-2024. Results show that the six operations exhibited nonlinear growth patterns for dispersion in both the target and control areas, with rapid expansion at the initial stage followed by a slower rate. The dispersion rate, distance, extent and concentration of the seeding agent vary significantly depending on the meteorological conditions, such as atmospheric turbulence, wind speed, stability and humidity. For the six operations, the vertically integrated liquid water content (VIL) showed notably high entropy weights (0.06-0.43) in multiple operations (No. 2, 3 and 6), making it a relatively stable indicator for evaluating the cloud seeding effects. Due to complex cloud microphysical processes such as latent heat release from deposition, downdrafts, cloud dissipation and cloud development, the responses of cloud-top temperature to seeding varied considerably (-44.56°C~-6°C). The effects of cloud seeding on cloud effective radius and optical thickness are complex and vary substantially depending on specific seeding conditions. The responses of liquid water path were time-dependent, the seeding-induced responses of radar reflectivity exhibited distinct patterns, including delayed manifestation, strong enhancement, and ineffectiveness or being masked. The strong-echo area and the VIL in the target areas fluctuated and generally decreased over time, respectively. The integrated physical inspection dimensionless index (PIDI) values for the seven indicators ranged from 15.0% to 69.7%, showing a smaller variation magnitude compared with the change rates of individual indicators, which reflects the synergistic effects of multiple indicators. This study provides a quantifiable and robust framework that mitigates the interference of natural variability, thereby advancing cloud seeding techniques and improving effect evaluation capabilities for artificial precipitation enhancement.

Keywords: Cloud seeding; Simulation of seeding agent transport and dispersion; Dimensionless processing; Entropy weight method; Physical evaluation of seeding effects

35 1. Introduction

Artificial precipitation enhancement via cloud seeding is a key technology for alleviating water scarcity, yet its effectiveness evaluation has long been challenged by the substantial natural variability of precipitation and the difficulty in separating the "artificial signal" (Zhang et al., 2010; Rauber et al., 2019). Traditional statistical approaches require a large volume of precipitation data spanning extended periods and are easily confounded by large natural variability, making it difficult to directly attribute observed effects to seeding operations (Li, 2002; Wu et al., 2015). In contrast, physical evaluation methods provides objective mechanistic evidence for cloud seeding by capturing cloud microphysical and dynamic responses, thereby enhancing the scientific validity and credibility of the evaluation (Flossmann et al., 2019; Wang et al., 2022). The core

https://doi.org/10.5194/egusphere-2025-4482 Preprint. Discussion started: 29 October 2025 © Author(s) 2025. CC BY 4.0 License.



55

60

65

70

80

85



significance of physical evaluation for seeding operation lies in three main aspects. Firstly, it scientifically validates the seeding effectiveness and underlying mechanisms. By quantifying the changes in cloud microphysical parameters induced by seeding and elucidating the macro- and micro-scale cloud processes involved, physical evaluation establishes a causal chain of "intervention-response-potential precipitation" (Jia and Yao, 2016; Wan et al., 2023). This approach helps prevent the misinterpretation of natural variability as seeding effects (Silverman, 2001) and provides essential physical support for statistical analyses (Rauber et al., 2019). Secondly, it offers critical guidance for optimizing seeding schemes. By determining optimal seeding parameters (i.e., clouding seeding altitude, temperature window, dosage and timing), the efficiency of precipitation enhancement can be improved. For instance, researches in the Qilian Mountains have reported that seeding at -3°C with an AgI release rate of 1.2 g·s⁻¹ achieved a precipitation enhancement efficiency of 10.4% (Ren et al., 2023), and confirmed the effectiveness of "seeding temperature window" and nucleation mechanism (Dong et al., 2022). Thirdly, it enhances the evaluation credibility and supports decision-making. The direct evidence provided by physical evaluation greatly strengthens the scientific persuasiveness of the seeding effect evaluation (WMO, 2015; Zhang et al., 2024). Combined with statistical methods, it offers robust support for decision-making in cloud water resource development. The World Meteorological Organization emphasizes that conclusions on cloud seeding can be considered credible only when cloud microphysical observational evidence and seeding outcomes mutually corroborate each other (Li, 2002; Wang et al., 2022).

The physical evaluation technique for cloud seeding can directly capture the evidence chain of "seeding agent dispersioncloud microphysical response-seeding effect" (Wu et al., 2018; Yan et al., 2024). Currently, this technique is characterized by three main features: comprehensive three-dimensional observations, refined numerical simulations and diversified evaluation methods. Three-dimensional observations on which physical evaluation relies typically involve cloud-seeding aircraft, Doppler or polarimetric weather radars, satellite remote sensing, and ground-based rain gauges. Specifically, cloud-seeding aircrafts are equipped with probes such as cloud droplet probe, cloud imaging probe, high-volume precipitation spectrometer and liquid water content probe, which are used to obtain cloud particle size spectra, number concentrations and cloud liquid water content (Dong et al., 2022; Yang et al., 2023). Doppler or polarimetric weather radars monitor key variables including reflectivity, hydrometeor phase, liquid water content and wind fields, allowing the tracking of seeding areas and associated precipitation (Geerts et al., 2010; Wang et al., 2021; Zheng et al., 2024). Satellite remote sensing supports the identification of supercooled water or ice crystal regions (Guo et al., 2023), and ground-based rain gauges record precipitation distribution within target areas (Wang et al., 2021). Additionally, ongoing innovations in cloud microphysics sampling techniques provide new evidence for physical evaluation. For example, high-volume membrane filters have significantly enhanced the sampling efficiency for ice nucleus (Grawe et al., 2023). Regarding refined numerical simulations, several studies have employed high-resolution cloud models and mesoscale models coupled with seeding modules to simulate the transport paths, dispersion extents and effective lifetimes of seeding agents (Yu et al., 2002; Sha et al., 2022). Numerical simulations have also been applied to evaluate the effects of artificial ice nuclei or giant cloud condensation nuclei on cloud microphysical properties and precipitation (Xue et al., 2013; Ren et al., 2023), as well as to compare precipitation differences between seeding and nonseeding scenarios (Wan et al., 2023). In terms of diversified evaluation methods, commonly used approaches include comparisons between target and control areas (Dong et al., 2022; Sha et al., 2022; Wang et al., 2024), analysis of downstream changes via tracking seeding plumes using radar or satellite (Wang et al., 2021), and quantitative evaluation of seeding effects through precipitation forecasting models based on deep learning or machine learning techniques, such as the algorithms of U-Net combined with Gated Recurrent Unit and random forest (Liu et al., 2023; Zhang et al., 2024).

Notable advances have been achieved in physical evaluation techniques for cloud seeding, encompassing observational validation and response mechanisms to seeding agents, optimization of seeding parameters and threshold conditions, elucidation of seeding mechanisms and dynamic feedback, as well as the development of evaluation methods and quantitative assessments. Previous studies have demonstrated that after cloud seeding, the cloud effective radius within the trajectory area increases while the optical thickness decreases (Yan et al., 2024). Additionally, radar reflectivity is enhanced by 10–15 dBZ, accompanied by elevated cloud tops, rightward shifts in cloud droplet spectra, and higher concentrations of large ice particles (>100 µm) (Dong et al., 2020; Guo et al., 2023). The release of AgI-type seeding agents markedly elevates ice crystal concentrations in the seeded area, concurrent with a decrease in liquid water content and an increase in ice water content (Dong et al., 2022). Substantial growth is also observed in ice crystals with diameters of 125–300 µm, with ice-crystal concentrations

https://doi.org/10.5194/egusphere-2025-4482 Preprint. Discussion started: 29 October 2025 © Author(s) 2025. CC BY 4.0 License.



90

95

100

105

110

115

120

125

130

135



in the region with high cloud droplet concentrations rising by up to 116-fold (Cui et al., 2024). The transformation of supercooled droplets to ice crystals is accompanied by a 20% increase in graupel content and a 22.9% enhancement in surface precipitation (Wan et al., 2023). Parameter optimization studies have shown that for experiments over the Qilian Mountains, seeding at the -3° C and -21° C layers yielded the most effective precipitation enhancement. A threshold effect was observed for the AgI seeding rate, where the precipitation enhancement rate stabilized at 10.4% when the seeding rate was 1.2 g·s⁻¹ and was suppressed when the seeding rate exceeded 1.5 g·s⁻¹ (Ren et al., 2023). Substantial differences in enhancement rates were also found among microphysical schemes, with the Milbrandt scheme yielding increases of 16.3%–24.7% compared with only 0.47%–1.38% for the Thompson scheme (Hua et al., 2024). Hua et al. (2024) proposed the concept of a "seeding window" and noted that snow particles induced by seeding required 154 minutes to enhance downwind precipitation, with an effective window of about 70 minutes. For evaluation, methods such as random forest and circulation-index-based precipitation classification models have been employed to identify effective seeding operations (Zhang et al., 2024).

Despite these advances, physical evaluation of cloud seeding still faces several critical bottlenecks. These include the interference of natural precipitation variability and the difficulty of signal separation, insufficient accuracy and coverage of observations, limitations in numerical models and mechanism understanding, a lack of standardized evaluation methods, and challenges in applying emerging technologies. Due to the high spatio-temporal variability of cloud-precipitation systems, seeding signal (precipitation enhancement) is easily masked by natural fluctuations (Wu et al., 2015), and it is difficult to find natural clouds with identical physical properties for comparison (Sha et al., 2022). Disturbances in wind fields can also displacement in the response area (Guo et al., 2023), further complicating the separation of seeding signal from natural variability. The limitations in cloud physics detection have greatly constrained the ability to evaluate cloud seeding effects. Specifically, for detection using meteorological satellites, the obtained cloud-top information struggles to accurately retrieve the vertical cloud structure. For detection based on meteorological radars, issues include blind zones in detection range, insufficient spatial resolution, and retrieval errors in physical quantities (Sha et al., 2022; Guo et al., 2023; Liu et al., 2023). For detection using cloud seeding aircrafts, limitations involve restricted coverage, a tendency of airborne probes to underestimate small ice crystal concentrations, and measurement interference caused by cloud and precipitation particle shattering (Lance et al., 2010; Cui et al., 2024). Additionally, uncertainties in numerical models and deficiencies in microphysical parameterization schemes lead to biases in precipitation simulation (Guo et al., 2006; Crawford et al., 2012). Errors in simulating the dispersion of seeding agents may arise from factors including initial conditions, sensitivity to atmospheric turbulence, activation timing of seeding agents, and the boundaries of affected areas [16]. The weak performance of multiscale coupling models linking cloud microphysics, mesoscale dynamics and synoptic-scale processes further limits the capability of physical evaluation for cloud seeding (Yoo et al., 2022). Due to the low correlation in parameters between target and control areas in non-uniform clouds (Wang et al., 2024), the evaluation generally relies on single indicators and lacks a framework that integrates microphysical-dynamic-precipitation responses (Rauber et al., 2019) or a comprehensive evaluation system for various indicators. Additionally, current evaluation of cloud seeding effects faces challenges in applying emerging technologies, such as insufficient seeding samples for deep learning and the risk of model overfitting (Liu et al., 2023).

To address these technical challenges, this study develops a comprehensive framework that integrates a series of key technologies to reduce attribution uncertainties and more effectively eliminate the influence of natural variability in physical evaluation, with the aim of providing a quantifiable and interference-reduced basis for physical evaluation of cloud seeding. The key technologies consist of dimensionless—entropy weight processing, high-precision simulation of seeding agent dispersion, dynamic similarity-based selection of control areas, and a multi-parameter integrated response index. Specifically, this study introduces dimensionless—entropy weight processing to scientifically quantify the weights of key cloud microphysical parameters in response to seeding agents and thereby identify dominant indicators, enabling intuitive quantification and standardized evaluation of the overall physical response to seeding operations. High-precision simulations of the three-dimensional transport paths, dispersion extent and concentration distribution of seeding agents are performed by using the Hybrid Single-Particle Lagrangian Integrated Trajectory (HYSPLIT) model, providing a precise spatial matching framework for physical response observations. Furthermore, the selection of dynamically similar control areas is optimized through the introduction of similarity measurement coefficients between the target (affected by cloud seeding) and control

https://doi.org/10.5194/egusphere-2025-4482 Preprint. Discussion started: 29 October 2025 © Author(s) 2025. CC BY 4.0 License.





areas, allowing for dynamic determination of the optimal control area and effectively mitigating the influence of natural variability in cloud-precipitation processes.

2. Materials and Methods

2.1. Data

140 The study area covers the region of 28N°-44°N, 106E°-124°E. Multi-source and multi-scale meteorological observations and reanalysis data are integrated to comprehensively evaluate the effects of cloud seeding operations. The datasets primarily consist of the following four categories. First is detection data by aircrafts for cloud seeding operations, which provide information on flight trajectories, seeding operation timings, seeding altitudes, seeding dosages, temperature of the seeding layers, and aircraft models. Second is the ERA5 reanalysis data by the European Centre for Medium-Range Weather Forecasts, 145 which offer large-scale and long-term background meteorological fields with spatio-temporal resolutions of 0.25°×0.25° and 1 hour and 37 levels from 1000 hPa to 1 hPa in the vertical direction. Specific variables used comprise cloud base height, three-dimensional wind fields, temperature profiles, total column cloud liquid water content, and hourly total precipitation. The supercooled liquid water content is derived by calculating the cloud liquid water content above the 0°C layer. Third is meteorological radar observation data, which provide high-temporal-resolution (6 minutes) information on the three-150 dimensional structure of seeded clouds. Key variables used include composite reflectivity, ≥ 30 dBZ echo area, and vertically integrated liquid water content (VIL). Final is the data from Fengyun-4A geostationary meteorological satellite, which offer continuous monitoring of large-scale cloud-top properties with spatial-temporal resolutions of 4 km and 4 minutes. Specific variables used include cloud-top temperature, cloud effective radius, optical thickness, liquid water path, and cloud phase. Notably, satellite data for operation 3 are unavailable and are thus not used in this study.

155 2.2. Technical framework

Figure 1 shows the technical framework for physical evaluation of cloud seeding effects in this study.





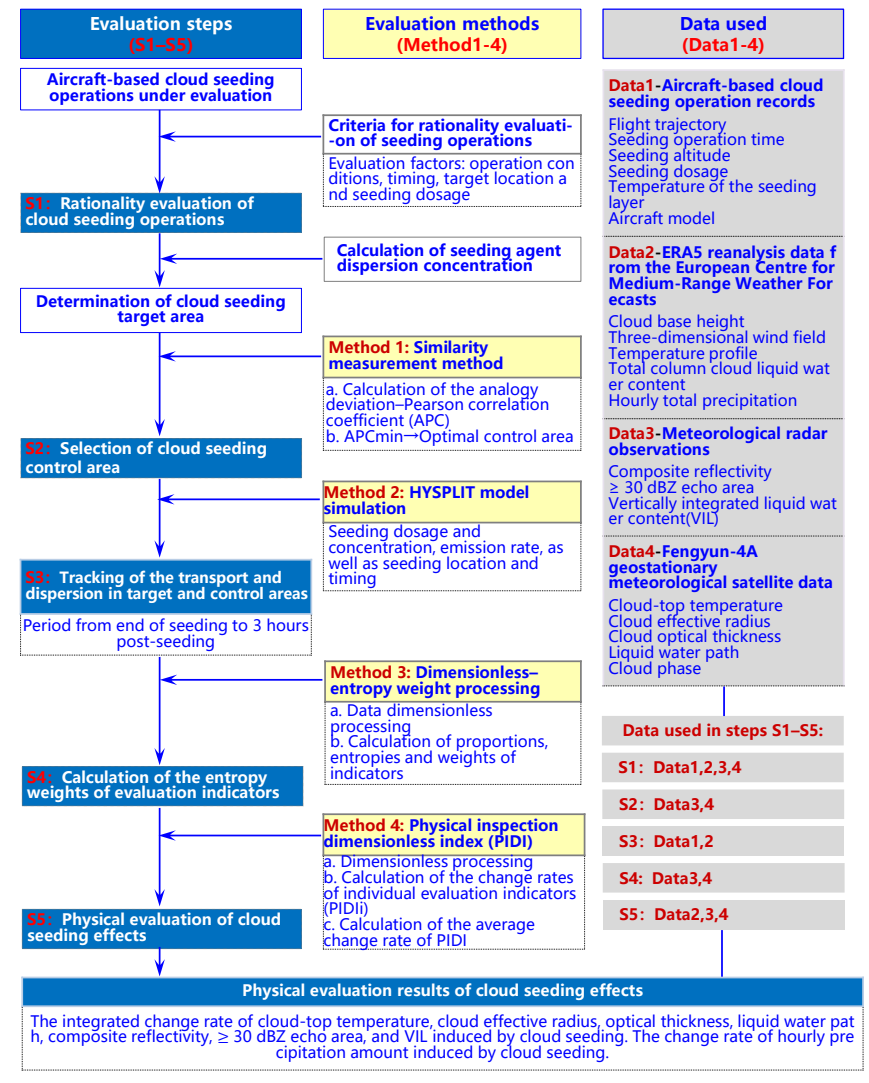


Figure 1: Technical flowchart of the physical evaluation algorithm for cloud seeding effects.

2.3. Main technical methods

160

165

170

2.3.1. Similarity measurement method (selection of cloud seeding control area)

To address the challenge of similarity discrimination in the process of selecting control areas for cloud seeding operation, this study introduces an analogy deviation—Pearson correlation coefficient (APC) method based on similarity measurement, which enhances the accuracy and stability of similarity discrimination between the target and control areas to a certain extent. The APC method integrates two key parameters, namely analogy deviation (C_{XY}) and Pearson correlation coefficient (ρ_{XY}), to comprehensively evaluate the similarity of two series of samples in terms of both numerical values ("value similarity") and variation trends ("shape similarity"), and concurrently reduce the influence of outliers. In Eqs. (1)–(6), X and Y represent two series of samples to be compared, and n is the data length. The value coefficient (D_{XY}) reflects the numerical difference between samples, while the shape coefficient (S_{XY}) characterizes the difference in curve shape. A smaller C_{XY} value indicates a higher similarity, and a larger ρ_{XY} value indicates a stronger positive linear correlation between the two series of samples (positive values indicate positive correlation). The APC is defined as the ratio of C_{XY} to ρ_{XY} , with smaller APC values (APC > 0)



185

190

195

200

205



(3)

indicating a higher similarity between samples. Finally, the composite APC value is determined by calculating the average APC value of multiple indicators, and the cloud with the minimum composite APC is selected as the optimal control area.

$$D_{XY} = \frac{1}{n} \sum_{k=1}^{n} |X_k - Y_k| \tag{1}$$

$$S_{XY} = \frac{1}{n} \sum_{k=1}^{n} \left| |X_k - Y_k| - \frac{1}{n} \sum_{k=1}^{n} |X_k - Y_k| \right|$$
 (2)

 $C_{XY} = \frac{1}{2}(D_{XY} + S_{XY})$

$$\rho_{XY} = \frac{\sum_{k=1}^{n} (X_k - \bar{X})(Y_k - \bar{Y})}{\sqrt{\sum_{k=1}^{n} (X_k - \bar{X})^2} \sqrt{\sum_{k=1}^{n} (Y_k - \bar{Y})^2}}$$
(4)

$$APC = \frac{C_{XY}}{\rho_{XY}} \tag{5}$$

$$APC = \frac{1}{m}(APC_1 + APC_2 + \dots ...APC_m)$$
(6)

2.3.2. HYSPLIT model simulation (tracking of the transport and dispersion of seeding agents in target and control areas)

Considering that the dispersion of cloud seeding agents essentially involves the transport and deposition of aerosol particles in the atmosphere, this study employs the HYSPLIT model to simulate the dispersion process of seeding agents. HYSPLIT model simulates the dispersion and trajectory of substances in the atmosphere, which is jointly developed by the National Oceanic and Atmospheric Administration (NOAA) of the United States and the Australian Bureau of Meteorology. It can simulates the trajectories of air masses, as well as the transport, dispersion and deposition of pollutants or tracers, featuring multi-scale adaptability (from local scales of a few kilometers to global scales) and multi-source input support (e.g., meteorological fields, topographical data and emission parameters). The simulation quantifies the dynamic distribution of the seeding agents on space through a concentration modeling, which follows a top-hat distribution vertically and a Gaussian distribution horizontally. The technical framework is based on Eq. (7), where Δc represents the concentration increment at a grid point contributed by a puff of mass m, m denotes the mass of pollutant released per unit time (i.e., source strength), σ_h is the horizontal dispersion coefficient, Δz represents the vertical height interval, and x is the horizontal distance from the point source to the calculation point.

$$\Delta c = m(2\pi\sigma_h^2 \Delta z)^{-1} exp(-0.5x^2/\sigma_h^2)$$
(7)

2.3.3. Entropy weight method (calculation of the entropy weights of evaluation indicators)

The first step of the entropy weight method is dimensionless processing. The observations X of multi-source evaluation indicators are standardized using min-max normalization. Specifically, for each indicator, the difference between its value and its minimum value is divided by the range of this indicator to eliminate the influence of units and magnitudes. In Eq. (8), X_{ij} denotes the parameter value for the i-th indicator at the j-th time point, and $\min(X_{ij})$ and $\max(X_{ij})$ represent the minimum and maximum values within the sample, respectively. X_{ij} represents the resulting dimensionless physical indicator, with values ranging from 0 to 1. The sample period covers from 1 hour before to 3 hours after the seeding operation, with data collected at 0.5-hour intervals.

$$X'_{ij} = \frac{X_{ij} - \min(X_{ij})}{\max(X_{ij}) - \min(X_{ij})}$$
(8)

Next, the proportions and entropy values for each indicator are calculated. In Eqs. (9) and (10), the proportion P_{ij} for the i-th indicator at the j-th time point is computed, followed by the calculation of the entropy value e_i for the i-th indicator, where n represents the number of data items.



215

220

230



$$P_{ij} = \frac{X'_{ij}}{\sum_{i=1}^{n} X'_{ij}} \tag{9}$$

$$e_i = \frac{-1}{\ln n} \sum_{i=1}^{n} (P_{ij} \ln P_{ij})$$
 (10)

The final step is to calculate the weight values. Using Eq. (11), the weight W_i for the i-th indicator is determined, where m denotes the number of indicators.

$$W_i = \frac{1 - e_i}{m - \sum_{i=1}^m e_i} \tag{11}$$

2.3.4 Physical inspection dimensionless index (PIDI) (physical evaluation of cloud seeding effects)

In this study, a physical inspection dimensionless index (PIDI) is introduced as a physical evaluation index for evaluating cloud seeding effects. By integrating multi-source observation parameters after dimensionless processing, the PIDI quantifies the overall variation trend and magnitude of all physical parameters involved in the evaluation. In Eqs. (12)–(14), X_{ij}' and Y_{ij}' denote the normalized values for the j-th sample of i-th indicator in the target area and the control area, respectively. r_{ij} represents the change rate for the i-th indicator at the j-th time point. PIDI_i is defined as the difference in average change rates between X_{ij}' and Y_{ij}' , reflecting the change rate of a given indicator attributable to cloud seeding in the target area. Since some evaluation indicators may exhibit positive change rates while others show negative change rates in different seeding operations, the absolute values of all PIDI_i are taken before averaging, so as to determine the overall change degree for all indicators.

$$r_{ij} = \left(\frac{X'_{ij} - X'_{(i-1)(j-1)}}{\Delta j} - \frac{Y'_{ij} - Y'_{(i-1)(j-1)}}{\Delta j}\right) \times 100\%$$
 (12)

$$PIDI_i = \frac{1}{n} \sum_{i=2}^n r_{ij} \tag{13}$$

$$PIDI = \frac{\sum_{i=1}^{m} (|PIDI_i| \cdot W_i)}{m}$$
 (14)

3. Results

225 3.1. Rationality evaluation of cloud seeding operations

Prior to effect evaluation, it is essential to conduct a rationality evaluation on seeding operation processes from aspects of operation conditions, timing, target location and seeding dosage. Only the cases that meet the criteria for rationality evaluation will proceed to physical evaluation. The criteria for rationality evaluation are summarized in Table 1. For this study, a total of twelve aircraft-based cloud seeding operations conducted in Henan Province of China during 2023–2024 were selected for rationality evaluation. The target cloud systems were stratiform or stratocumulus cold clouds, and cold-cloud catalysts were used as seeding agents. Of these twelve operations, only six satisfied the rationality criteria and were selected for further evaluation. Operation details of the six operations are summarized in Table 2, and the corresponding flight paths, overlaid with radar reflectivity in both plan view and vertical cross-section, are presented in Fig. 2.

Table 1. Criteria for rationality evaluation of cloud seeding operations.

Evaluation elements

Evaluation requirements

(1) The cloud system to be seeded should be stratiform or stratocumulus clouds.
(2) The cloud system to be seeded should have sustained moisture transport and precipitation potential.

Operation timing

(1) The cloud to be seeded should contain a certain amount of supercooled water.





	(2) The cloud to be seeded should contain relatively high moisture content	
	and liquid water content.	
	(3) Cloud-top temperature should be below −10°C.	
	(1) The cloud to be seeded should meet the seeding temperature window.	
Target location	(2) The flight path should be reasonably designed to form a large-area	
	surface source seeding.	
C1: 1	The seeding dosage should be reasonable and be sufficient for dispersion	
Seeding dosage	(seeding agent concentration greater than or equal to $10 \cdot L^{-1}$).	

Table 2. Details of aircraft-based seeding operations that meet the rationality criteria.

Operation number	Operation date (yy-mm- dd)	Takeoff/lan ding airport			Seeding period (UTC)	Seeding duration (hours)	Average seeding height (km)	Number of AgI smoke sticks used	υ
1	2023-03-16	Xinzheng Airport	King Air	B-124M	03:43-05:50	2.1	6.7	/	16
2	2023-04-02	Xinzheng Airport	King Air	B-124M	08:32-09:58	1.4	4.5	/	22
3	2024-03-23	Shangjie Airport	Y-12	B-12QH	01:20-03:45	2.4	4.9	20	/
4	2024-10-17	Shangjie Airport	Y-12	B-12QH	01:16-03:05	1.8	4.7	18	/
5	2024-10-17	Shangjie Airport	Y-12	B-12QH	05:51-08:33	2.7	4.6	22	/
6	2024-10-20	Shangjie Airport	Y-12	B-12QH	06:56-08:32	1.6	4.7	18	/

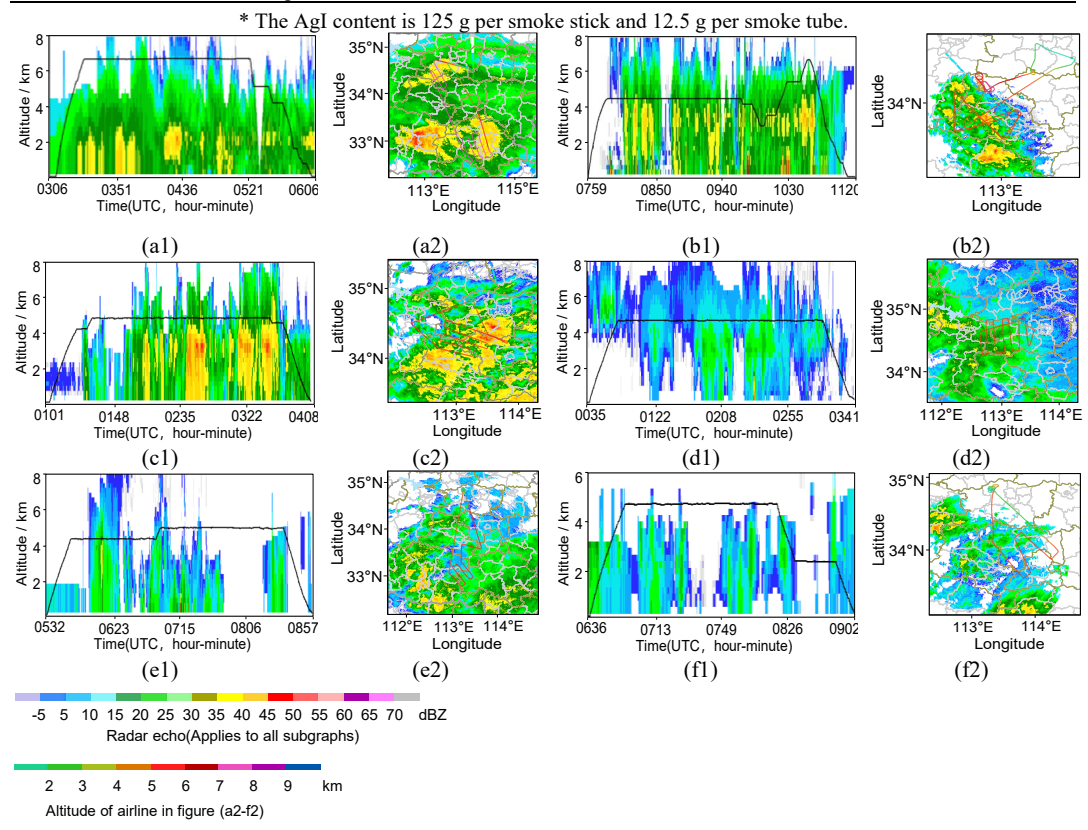


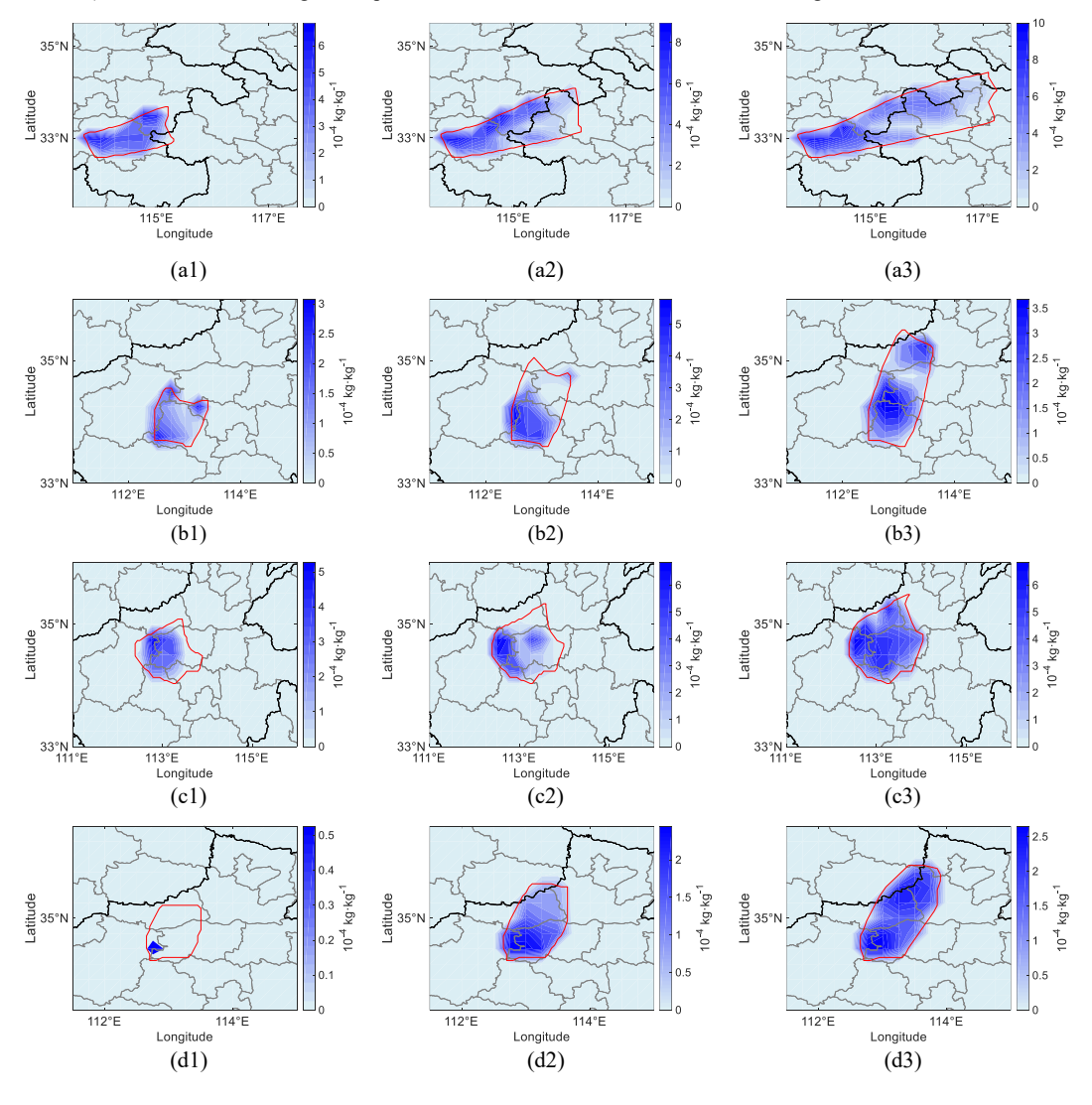
Figure 2: Flight paths of the six aircraft-based cloud seeding operations (solid black lines) overlaid with radar reflectivity in (a1,b1,c1,d1,e1,f1) plan view and (a2,b2,c2,d2,e2,f2) time-height cross-section.



245



According to the condition of supercooled water specified at the operation timing for rationality evaluation, ERA5 reanalysis data on pressure levels were used to calculate the distribution of supercooled water content, and to analyze the hourly supercooled water conditions within the target area during the three hours after cloud seeding (Fig. 3). It is evident that the supercooled water content was relatively abundant in the seeding areas for all six operations, meeting the requirements of rationality evaluation. Notably, substantial differences were observed among operations in initial conditions and post-seeding variations of supercooled water. For instance, Operation No. 4 exhibited an extremely low initial value (0.22 kg·kg⁻¹). Furthermore, some cases showed a continuous decrease (Operation No. 1), a continuous increase (Operation No. 3 and No. 5), or a fluctuating pattern (Operation No. 2 and No. 6) in supercooled water content after seeding. Most cases (Operation No. 1, 3, 4 and 5) exhibited notable changes in supercooled water content within 3 hours after seeding.





255

260

265



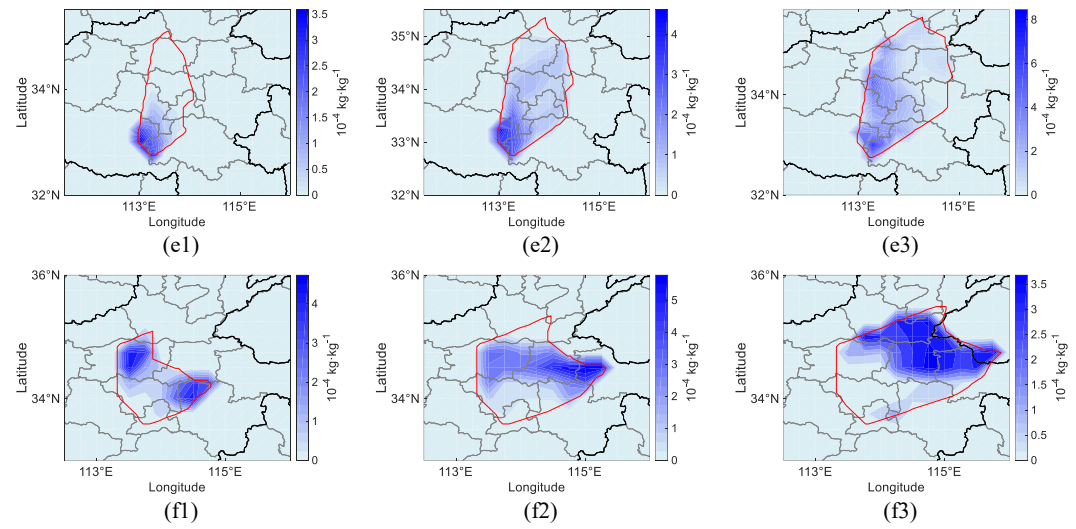


Figure 3: Distributions of hourly supercooled water content within the target area during the three hours after seeding for six operations (a1-a3, b1-b3, c1-c3, d1-d3, e1-e3, f1-f3). Red lines indicate the boundaries of the target area 1 hour, 2 hours and 3 hours after seeding.

3.2 Selection of cloud seeding control area

Based on the flight paths of the six cloud seeding operations, target areas were determined. Four control areas were preliminarily selected according to the cloud properties near the target areas. The APC method was used to select the optimal control area. The APC values for the four control areas and the optimal control area for each operation are listed in Table 3.

Table 3. Analogy deviation-Pearson correlation coefficient (APC) values for preliminary control areas and the selected optimal control areas for the six aircraft-based cloud seeding operations.

Operation		APC v	Optimal control area (with		
number	Control area 1	Control area 2	Control area 3	Control area 4	minimum APC value)
1	5.33	44.1	17.8	2.56	Control area 4
2	30.02	9.6	7.12	4.7	Control area 4
3	25.43	7.67	16.79	31.81	Control area 3
4	9.66	10.81	27.5	19.64	Control area 1
5	2.35	5.94	35.2	11.98	Control area 1
6	12.2	10.67	27.34	25.56	Control area 2

3.3 Tracking of the transport and dispersion of seeding agents in target and control areas

To trace the evolution of both target and control areas after seeding operations, the concentration modeling of the HYSPLIT model was applied to simulate the transport and dispersion of seeding agents in the target regions and the movement of cloud systems in the control areas during the three hours after seeding (Fig. 4). The simulations demonstrate several features. In both areas, the dispersion follows a nonlinear growth pattern, with a rapid expansion during the early stage and a slower rate thereafter, reflecting the influence of atmospheric turbulence or wind fields. In terms of horizontal dispersion, the seeding agent plumes extend along the prevailing wind direction, and the affected area gradually expands. The dispersion rate of seeding agents is also strongly influenced by meteorological factors such as wind speed, atmospheric stability, turbulence intensity and atmospheric humidity, resulting in considerable differences in dispersion rate, distance, extent and concentration among operations. Furthermore, the dispersion of seeding agents remains relatively confined within the initial release areas.



275



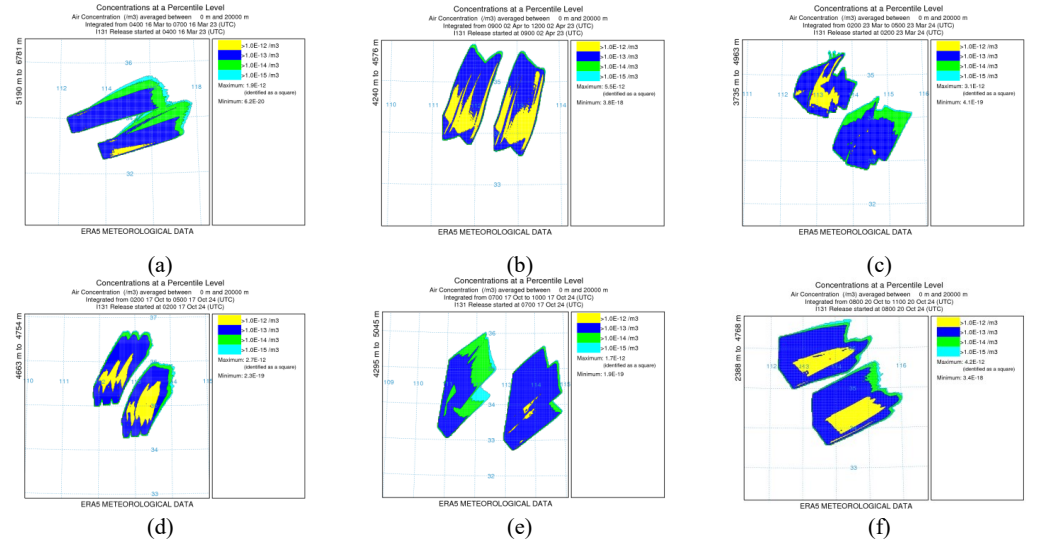
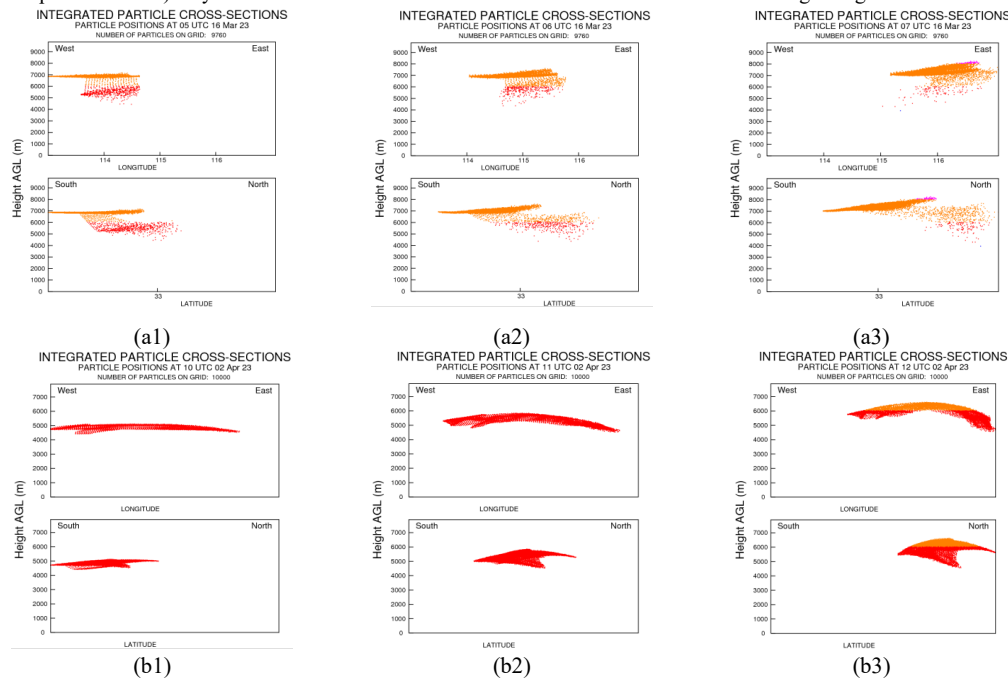


Figure 4: Simulations of the transport and dispersion of seeding agents in the target areas and the movement of cloud systems in the control areas during the three hours after seeding for six operations (a-f).

The concentration modeling of the HYSPLIT model was employed to obtain the vertical distribution of seeding particles. The hourly vertical dispersion patterns for the 3 hours after seeding are shown in Fig. 5. It is evident that the dispersion rate varies remarkably among operations due to the influence of meteorological conditions such as seeding dosage, wind speed at the seeding layer, atmospheric stability, turbulence intensity and atmospheric humidity. Rapid dispersion (as observed in Operation No. 3 and No. 6) is likely related to atmospheric instability or strong dynamical processes, whereas slow dispersion (as in Operation No. 4) may have been associated with stable stratification or insufficient seeding dosage.







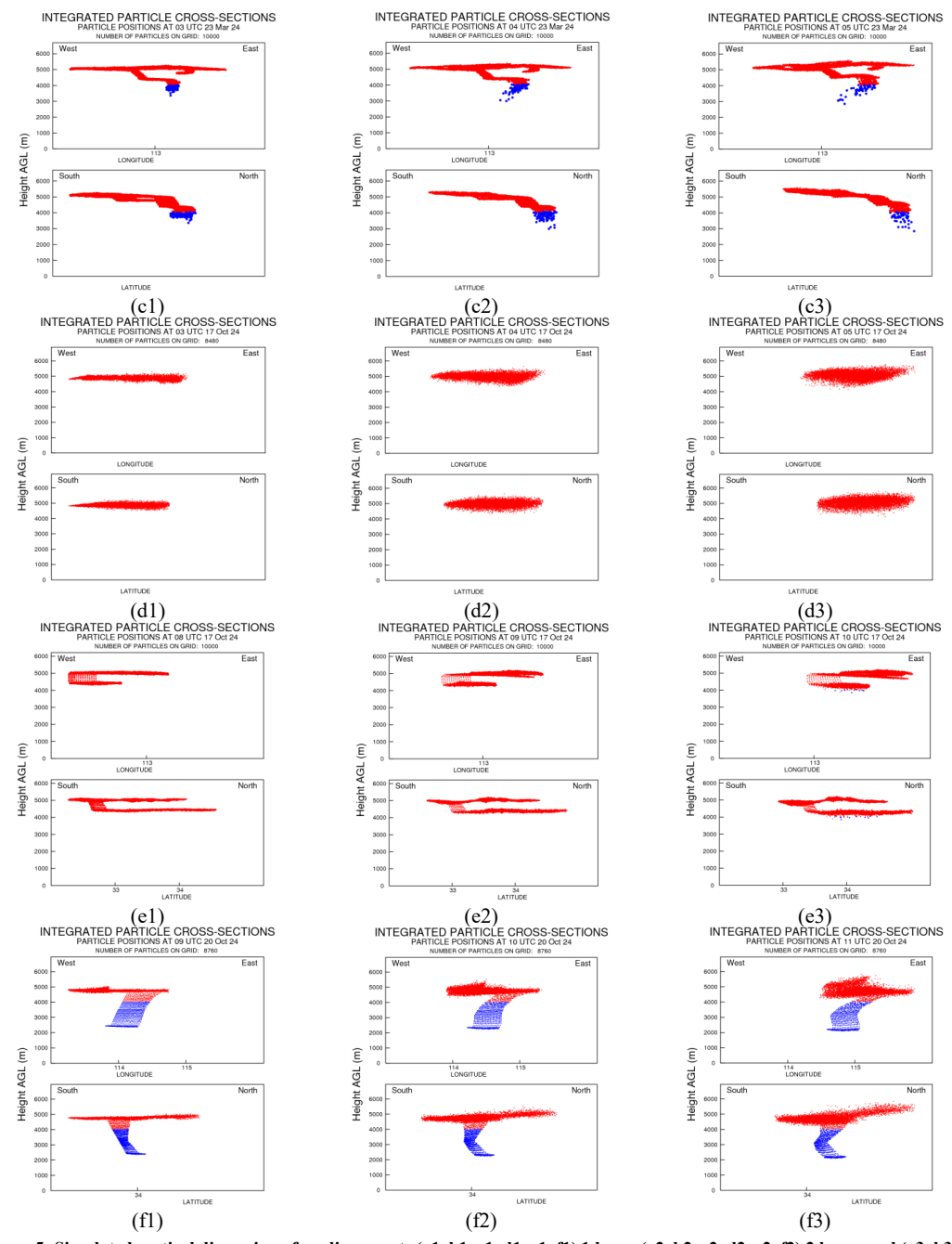


Figure 5: Simulated vertical dispersion of seeding agents (a1, b1, c1, d1, e1, f1) 1 hour, (a2, b2, c2, d2, e2, f2) 2 hours and (a3, b3, c3, d3, e3, f3) 3 hours after the moment when the seeding ends for six operations. Different colors represent different altitudes, and the density of scatter points indicates particle concentration.

Based on the transport and dispersion patterns in the target and control areas obtained by the HYSPLIT model simulations, a three-dimensional geospatial configuration of the flight paths as well as the hourly target and control areas during the three hours after seeding was established (Fig. 6).



290

295

300



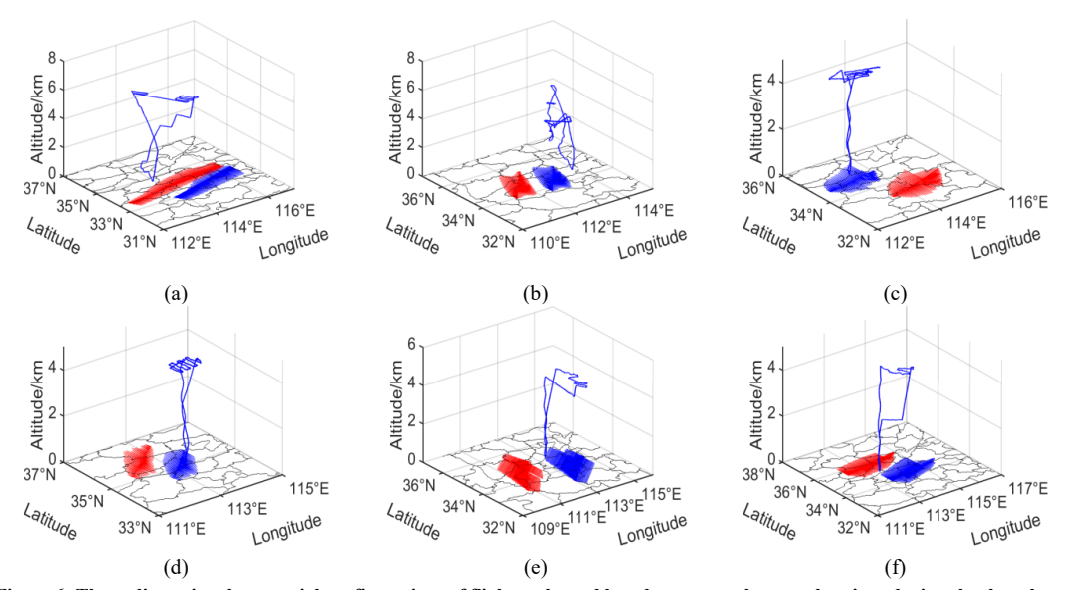


Figure 6: Three-dimensional geospatial configurations of flight paths and hourly target and con-trol regions during the three hours after seeding for six operations(a-f). Solid blue lines denote the flight paths of the seeding aircraft. Blue and red shaded areas represent the projections of the aerial target and control areas onto the ground, respectively.

3.4 Calculation of the entropy weights of evaluation indicators

For the six operations, entropy weights were calculated for various cloud microphysics-based evaluation indicators. The top seven most sensitive indicators were selected, namely cloud-top temperature, cloud effective radius, optical thickness, liquid water path, radar reflectivity, ≥ 30 dBZ echo area, and VIL. Entropy weights for these seven indicators were then recalculated and are listed in Table 4. Considerable differences are found in the entropy weights of the seven indicators across six operations, indicating that the dominant response indicators differed from case to case. Specifically, the entropy weights are 0.06-0.42 for cloud-top temperature, 0.14-0.24 for cloud effective radius, 0.12-0.25 for optical thickness, 0.14-0.29 for liquid water path, 0.05-0.38 for radar reflectivity, 0.08-0.27 for the ≥ 30 dBZ echo area, and 0.06-0.43 for the VIL. Notably, cloud-top temperature carries a relatively high weight in some cases (Operations No. 5 and 6). The VIL exhibits notably high weights in several operations (Operations No. 2, 3 and 6), suggesting that it might be a relatively stable and generally important indicator for evaluating cloud seeding effects. Nonetheless, limitations in satellite observations for some operations have affected the accuracy of multi-indicator synergy analysis, underscoring the need for improved observational datasets in future studies to enhance evaluation reliability.

Table 4. Entropy weights of evaluation indicators for the six operations.

Operation	Cloud-top	Cloud effective	Optical	Liquid water	Radar	≥ 30 dBZ echo	VIL
number	temperature	radius	thickness	path	reflectivity	area	VIL
1	0.06	0.24	0.12	0.14	0.16	0.12	0.15
2	0.21	/	/	/	0.25	0.17	0.37
3	/	/	/	/	0.38	0.19	0.43
4	0.13	0.14	0.25	0.29	0.05	0.08	0.06
5	0.42	/	/	/	0.14	0.22	0.23
6	0.30	/	/	/	0.15	0.27	0.27

3.5 Physical evaluation of cloud seeding effects

3.5.1 Individual evaluation indicators in the target and control areas

1.Cloud-top temperature

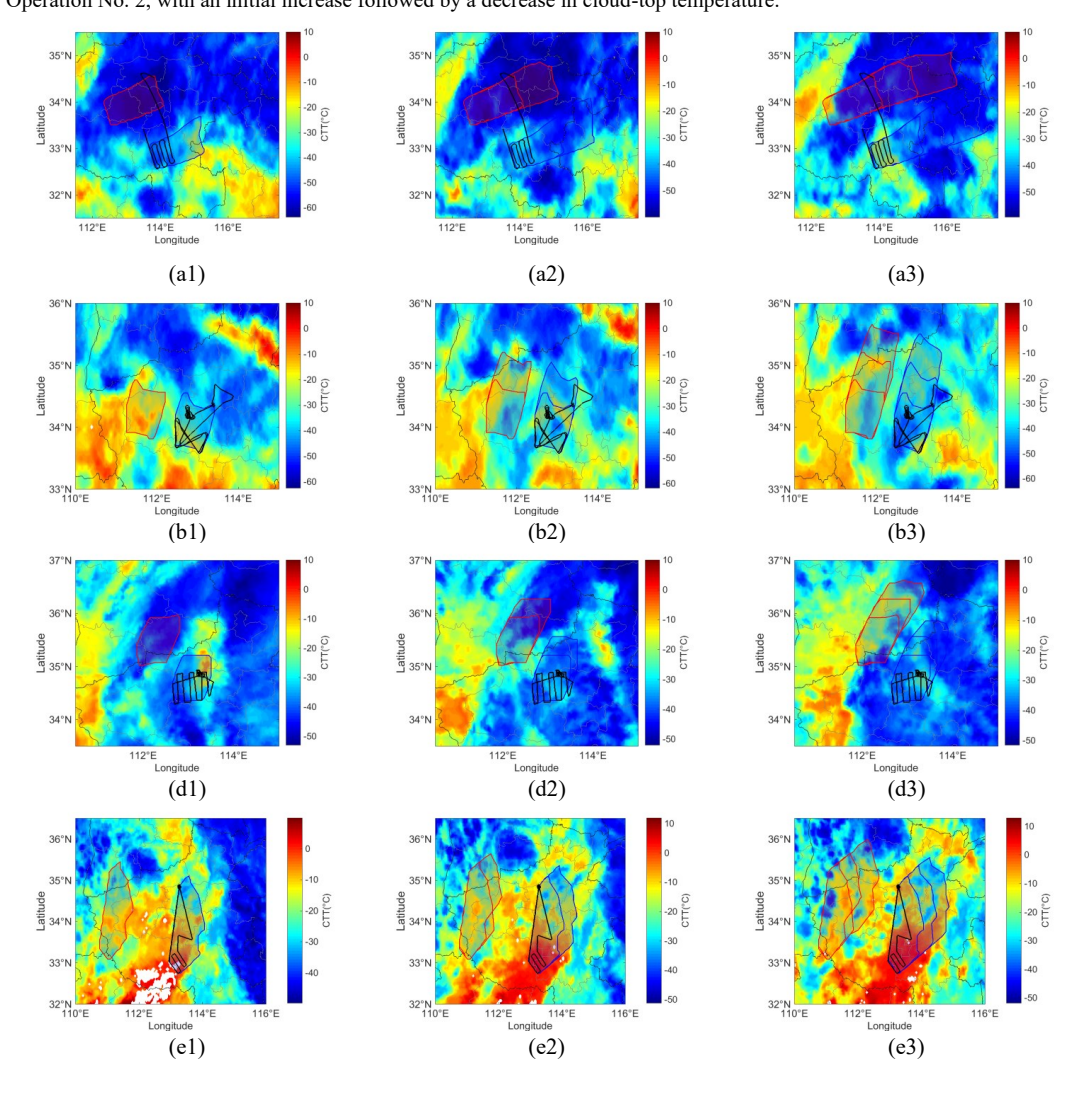


310

315



As displayed in Fig. 7 and Table 5, the changes of cloud-top temperature in the target and control areas during 1–3 hours after cloud seeding and the corresponding area-averaged hourly values are analyzed to elucidate the responses of cloud-top temperature to seeding. Across five operations, the mean cloud-top temperature in the target areas ranged from –44.56°C to –6°C. Due to the complex cloud microphysical processes, such as latent heat release from deposition (warming), cloud development (cooling), downdrafts (warming) and cloud dissipation (warming), the cloud-top temperature responses in the target areas varied markedly among different operations. In Operations No. 1, 4, 5 and 6, the cloud-top temperature in the target areas remained consistently higher than that in the control areas, whereas it was consistently lower in Operation No. 2. In Operations No. 1 and 4, the cloud-top temperature in the target areas decreased continuously, possibly reflecting cloud development or water vapor depletion due to precipitation. In contrast, Operations No. 5 and 6 exhibited a consistent increase in cloud-top temperature, likely resulting from seeding-induced downdrafts. Meanwhile, a weaker response was observed in Operation No. 2, with an initial increase followed by a decrease in cloud-top temperature.







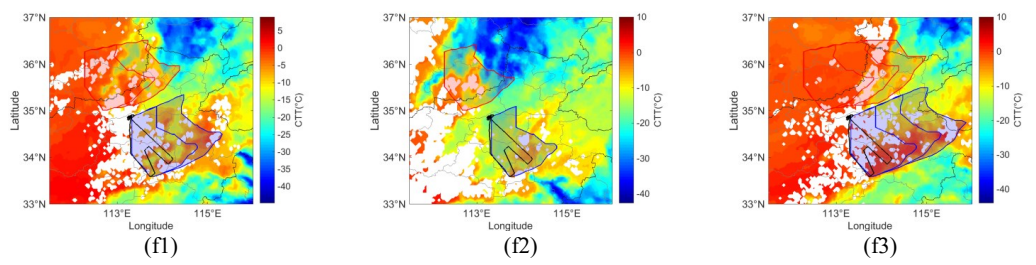


Figure 7: Flight paths and cloud-top temperature overlaid with target and control areas (a1, b1, d1, e1, f1) 1 hour, (a2, b2, d2, e2, f2) 2 hours and (a3, b3, d3, e3, f3) 3 hours after seeding for the six operations. Blue and red lines represent the boundaries of target and control areas, respectively.

Table 5. Area-averaged hourly cloud-top temperature in the target and control areas after seeding operations.

Operation number	Time point (hour)	Area-averaged cloud-top temperature in target areas (°C)	Area-averaged cloud-top temperature in control areas (°C)
	1	-33.12	-59.84
1	2	-41.47	-56.18
	3	-44.56	-51.91
	1	-34.81	-20.34
2	2	-31.59	-27.15
	3	-34.69	-32.47
	1	-26.99	-42.84
4	2	-34.27	-39.11
	3	-35.05	-30.19
	1	-16.39	-17.04
5	2	-13.53	-19.76
	3	-12.09	-19.66
	1	-10.82	-19.96
6	2	-8.81	-12.36
	3	-6.00	-6.83

2.Cloud effective radius

320

325

330

335

It should be noted that the visible and near-infrared channels of the Fengyun-4A satellite rely on sunlight to acquire signals, making it impossible to obtain valid inputs during nighttime. Meanwhile, the data retrieval accuracy at the infrared channel is insufficient and cannot replace the information provided by shortwave spectra. This technical limitation is particularly pronounced during dawn/dask periods or in high-latitude winters. Therefore, three indicators of cloud effective radius, optical thickness and liquid water path in Fengyun-4A satellite products are unavailable from evening to nighttime. Since several cloud seeding operations in this study (Operations No. 2, 3, 5 and 6) were conducted during evening or nighttime hours, the abovementioned three indicators were excluded from the evaluation process for these operations.

Similar to cloud-top temperature, the responses of cloud effective radius to cloud seeding were further examined (Fig. 8, Table 6) for the remaining two operations (No. 1 and 4), as shown in Fig. 8 and Table 6. In the target areas, the mean values of cloud effective radius ranged from 14.68 to 30.37 µm for the two operations. Specifically, in Operation No. 1, the cloud effective radius increased with time in both areas but remained consistently lower in target areas, suggesting that seeding may have suppressed cloud particle growth but promoted an increase in particle number concentration through mechanisms such as introducing condensation nuclei that compete for water vapor. In Operation No. 4, the effective radius in the target areas was initially larger than that in the control areas, but the difference gradually diminished over time, indicating that seeding may have enhanced the condensation or collision–coalescence processes and thereby accelerates early cloud particle growth. These contrasting results highlight the complexity of cloud seeding effects on cloud effective radius, with outcomes varying depending on seeding conditions.



345

350



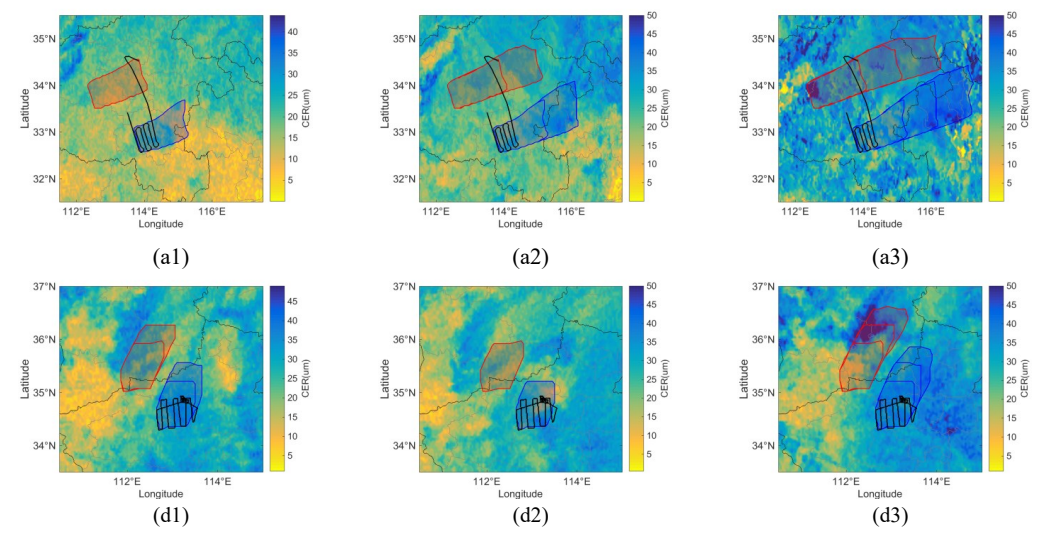


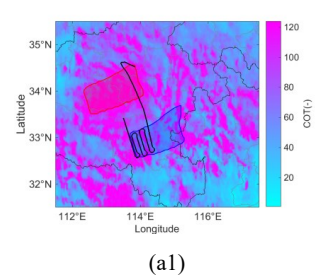
Figure 8: Flight paths and cloud effective radius overlaid with target and control areas (a1, d1) 1 hour, (a2, d2) 2 hours and (a3, d3) 3 hours after seeding for Operations No. 1 and 4. Blue and red lines represent the boundaries of the target and control areas, respectively.

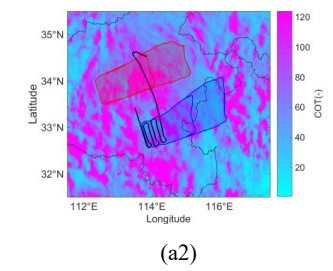
Table 6. Area-averaged hourly cloud effective radius in the target and control areas after seeding operations.

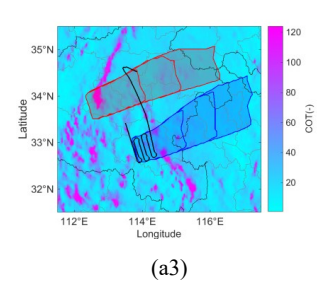
Operation	Time point	Area-averaged cloud effective	Area-averaged cloud effective radius
number	(hour)	radius in the target areas (μm)	in the control areas (μm)
	1	14.68	15.51
1	2	21.11	21.58
	3	30.37	32.28
	1	26.99	23.64
4	2	25.63	23.93
	3	29.48	29.16

3.Optical thickness

Likewise, the responses of optical thickness to cloud seeding were investigated (Fig. 9 and Table 7). In the two operations (No. 1 and 4), the mean optical thickness in the target areas ranged from 39.91 to 81.11. In both operations, the optical thickness in the target areas remained consistently lower than that in the control areas. In Operation No. 1, the optical thickness in the target areas decreased with time, suggesting that seeding may decrease cloud thickness or density through reducing the concentrations of cloud droplets or ice crystals. In contrast, in Operation No. 4, the optical thickness increased over time, possibly due to the ice—liquid phase change within clouds or cloud structure changes. These contrasting behaviors indicate that seeding may influence optical thickness by modifying cloud microphysical properties, highlighting that further investigation should incorporate additional meteorological parameters.









360

365



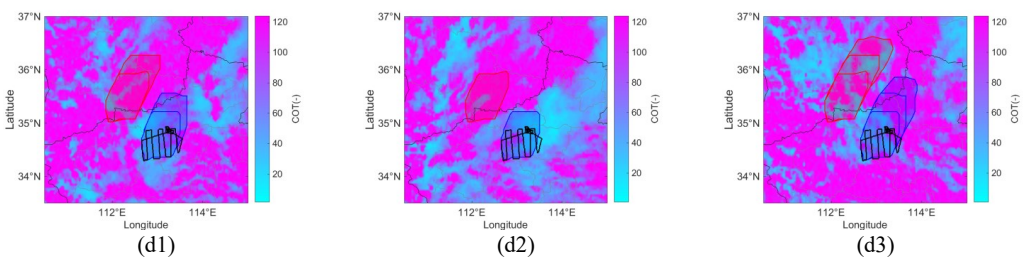


Figure 9: Same as Fig. 8, but for optical thickness.

Table 7. Area-averaged hourly optical thickness in the target and control areas after seeding operations.

Operation	Time point	Area-averaged optical thickness in	Area-averaged optical thickness in
number	(hour)	the target areas (dimensionless)	the control areas (dimensionless)
	1	77.73	103.42
1	2	76.81	98.77
	3	39.91	49.47
	1	50.82	117.12
4	2	60.86	106.52
	3	81.11	88.15

4.Liquid water path

The responses of liquid water path to seeding were also analyzed based on the changes in liquid water path in the target and control areas during 1–3 hours after cloud seeding (Fig. 10) and the area-averaged hourly values of liquid water path (Table 8). In the two operations (No. 1 and 4), the mean liquid water path in the target areas ranged from 733.65 to 1579.05 mm. The seeding effects on liquid water path appeared in a time-dependent pattern, with more pronounced effects during the first 1–2 hours after seeding and a tendency toward stabilization after 3 hours. In Operation No. 1, the liquid water path in the target areas was consistently lower than that in the control areas, reaching its peak in the second hour after seeding yet remaining considerably lower than the control value. In Operation No. 4, the liquid water path in the target areas was markedly lower than that in the control areas during the first 1–2 hours after seeding, but the two values were close in the third hour, suggesting that the responses of liquid water path to seeding weakened over time or that the regional differences decreased.

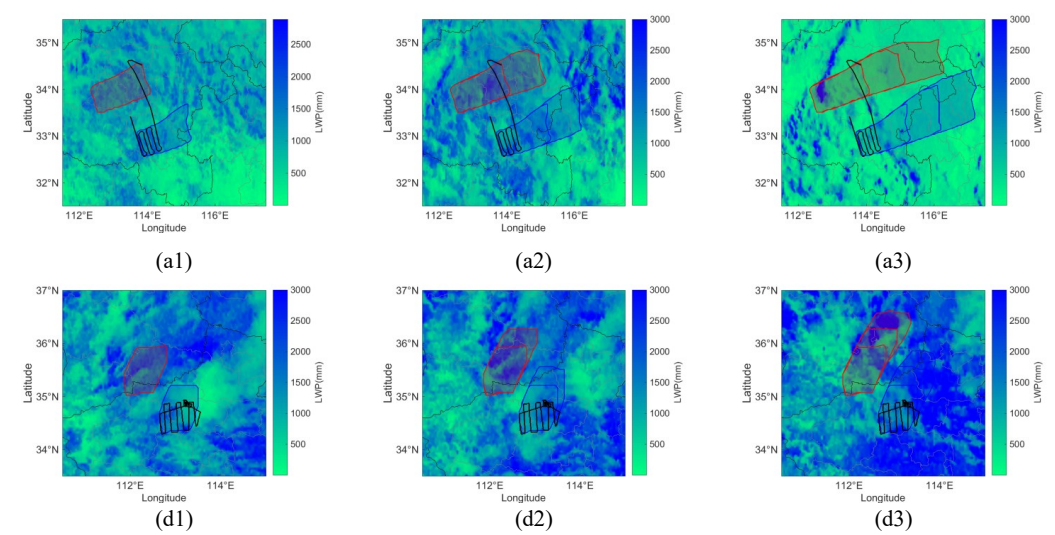


Figure 10: Same as Fig. 8, but for liquid water path.

Table 8. Area-averaged hourly liquid water path in the target and control areas after seeding for Operations No. 1 and 4.

Operation number	Time point (hour)	Area-averaged liquid water path in the target areas (mm)	Area-averaged liquid water path in the control areas (mm)
1	_ 1	733.65	1063.79



375

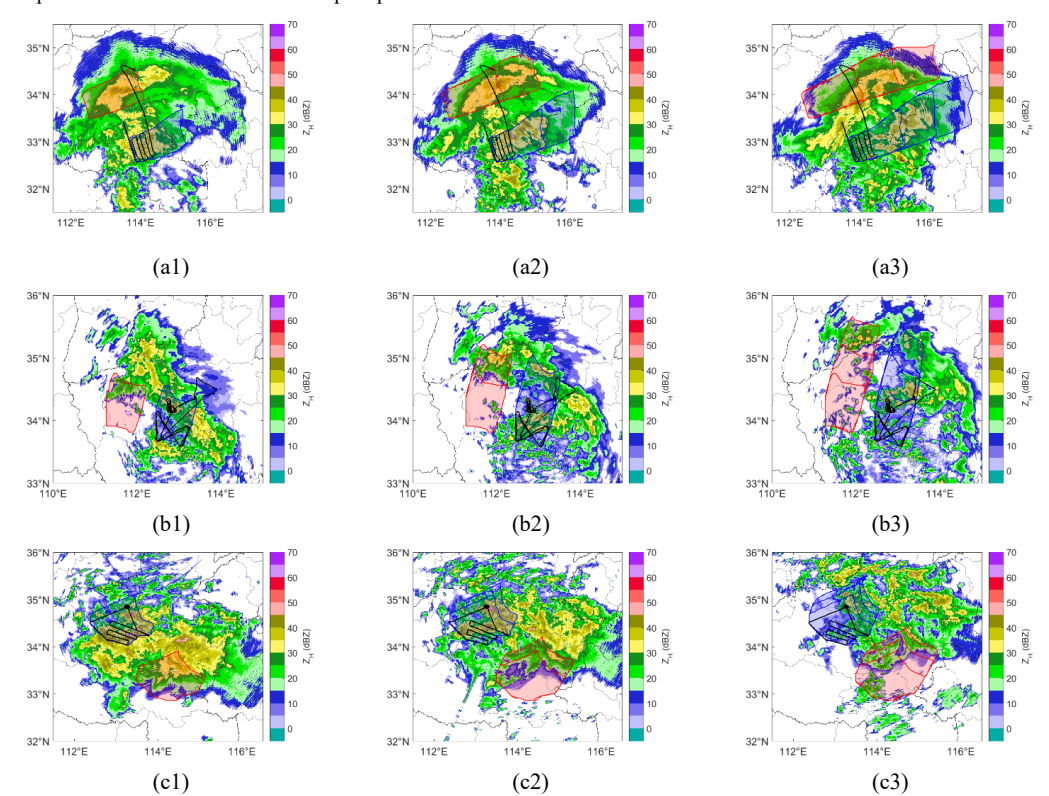
380



	2	1046.80	1398.87
	3	790.87	1047.52
	1	898.68	1844.08
4	2	1033.13	1681.91
	3	1579.05	1693.68

5. Radar reflectivity

As illustrated by Fig. 11 and Table 9, the responses of radar reflectivity to cloud seeding were analyzed. Across the six operations, the mean radar reflectivity in the target areas ranged from 6.35 to 15.06 dBZ. The seeding-induced responses exhibited multiple patterns among different operations, including delayed manifestation (Operations No. 1 and 3), strong enhancement (Operation No. 2), and ineffectiveness or being masked (Operations No. 4 and 6). In Operations No. 1 and 3, the radar reflectivity in the target areas was initially lower than that in the control areas but later surpassed it, suggesting that early-stage seeding effect was insufficient and displaying a delayed effect in the later period. This implies that longer evaluation periods may be required to fully capture seeding effects. In Operation No. 2, the radar reflectivity in the target areas was consistently higher than that in the control areas, indicating that cloud seeding enhanced cloud condensation. This favorable cloud condition (e.g., high supercooled water content) suggests high seeding efficiency. In contrast, in Operation No. 4, the radar reflectivity in the target areas remained consistently lower than that in the control areas, possibly due to unfavorable cloud conditions (e.g., insufficient ice crystals) or the masking of seeding effects by stronger natural precipitation in the control areas. Similarly, during Operation No. 6, the radar reflectivity in the target areas was markedly lower than that in the control areas during the first hour after seeding. In this case, the seeding effects may be masked, making the evaluation results more susceptible to interference from natural precipitation.







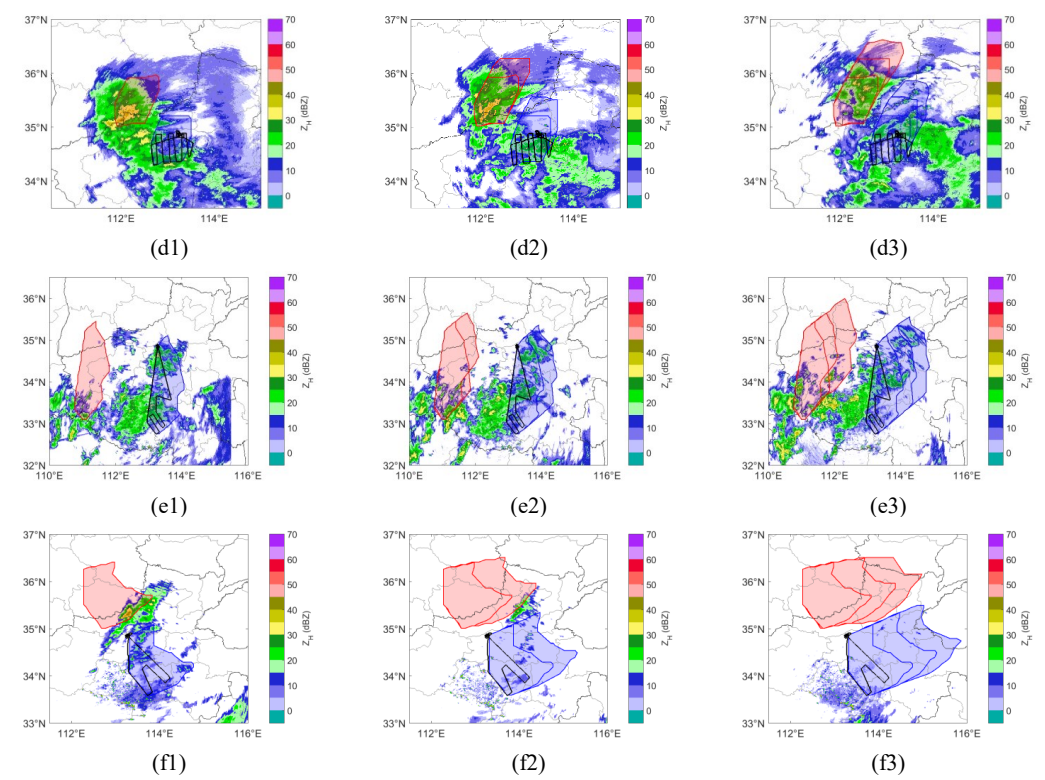


Figure 11: Same as Fig. 7, but for radar reflectivity.

Table 9. Area-averaged hourly radar reflectivity in the target and control areas after seeding operations.

Operation number	Time point (hour)	Area-averaged radar reflectivity in the target areas (dBZ)	Area-averaged radar reflectivity in the control areas (dBZ)
	1	26.16	28.61
1	2	24.29	27.74
	3	24.57	24.22
	1	24.82	17.69
2	2	21.96	20.84
	3	19.70	18.43
	1	27.36	29.06
3	2	28.57	22.37
	3	22.29	18.41
	1	14.15	19.10
4	2	14.49	19.00
	3	13.11	16.99
	1	14.69	9.66
5	2	15.06	12.12
	3	13.30	12.29
	1	8.80	19.12
6	2	8.25	18.68
	3	6.35	7.96

385 6.Strong echo (≥ 30 dBZ) area

Table 10 lists the statistical results of the strong-echo (\geq 30 dBZ) area in target and control areas. It is found that the mean strong-echo area in the target areas ranged from 2 to 225 km² across the six operations, which fluctuated over time. Specifically, in Operations No. 1 and No. 3, the strong-echo area increased and then decreased, while in the remaining four operations (No.



395

400

405



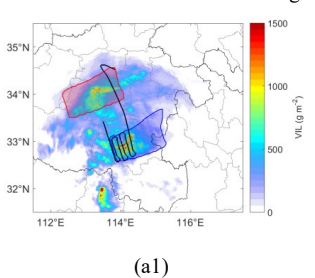
2, 4, 5 and 6), no distinct pattern was observed. In Operations No. 1 and No. 3, the strong-echo area in the target regions was consistently smaller than that in the control areas, indicating that cloud seeding had not markedly increase the strong-echo area. In contrast, in Operation No. 2, the strong-echo area in the target areas was notably larger than that in the control areas, implying a possible local enhancement effect. While in Operations No. 4, 5 and 6, the strong-echo area in the target areas was considerably smaller than that in the control areas, possibly due to limitations by cloud microphysical properties under natural atmospheric conditions.

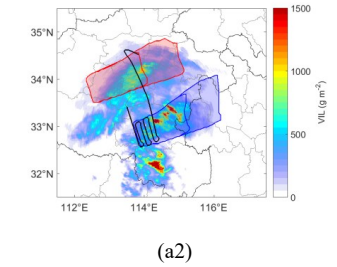
Table 10. Area-averaged hourly strong-echo (≥ 30 dBZ) area in the target and control areas after seeding operations.

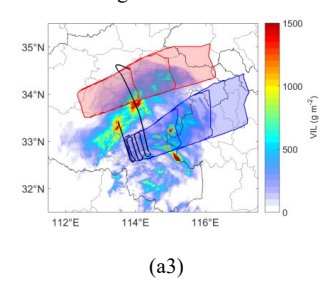
Operation number	Time point (hour)	Area-averaged strong-echo area in the target areas (km2)	Area-averaged strong-echo area in the control areas (km²)
number	1	2716	3968
1	2	5667	7246
•	3	7724	7804
	1	1493	214
2	2	2185	989
	3	1998	799
	1	4010	5346
3	2	6321	3273
	3	3513	762
	1	17	920
4	2	95	883
	3	87	463
	1	177	0
5	2	225	36
	3	48	106
	1	4	436
6	2	2	219
	3	6	0

7. Vertically integrated liquid water content

As illustrated by Fig. 12 and Table 11, the changes in the VIL in the target and control areas during 1-3 hours after seeding and the area-averaged hourly VIL values are employed to analyze the responses of VIL to cloud seeding. Across the six operations, the mean VIL in the target areas ranged from 0.81 to 695.27 g·m⁻². Overall, the VIL in the target areas decreased over time, likely due to natural precipitation processes or the water depletion within clouds after seeding. In Operations No. 2, 3 and 5, the VIL in the target areas was notably higher than that in the control areas. However, the situation was almost opposite in Operations No. 4 and 6, where the VIL was almost always lower than that in the control areas. In Operation No. 1, the VIL in the target areas was lower than that in the control areas during the first 1-2 hours after seeding but exceeded that in the control areas in the later period. In Operation No. 2, the VIL in the target areas decreased over time. In Operation No. 3, the difference in the VIL between the target and control areas decreased in the later period after seeding.











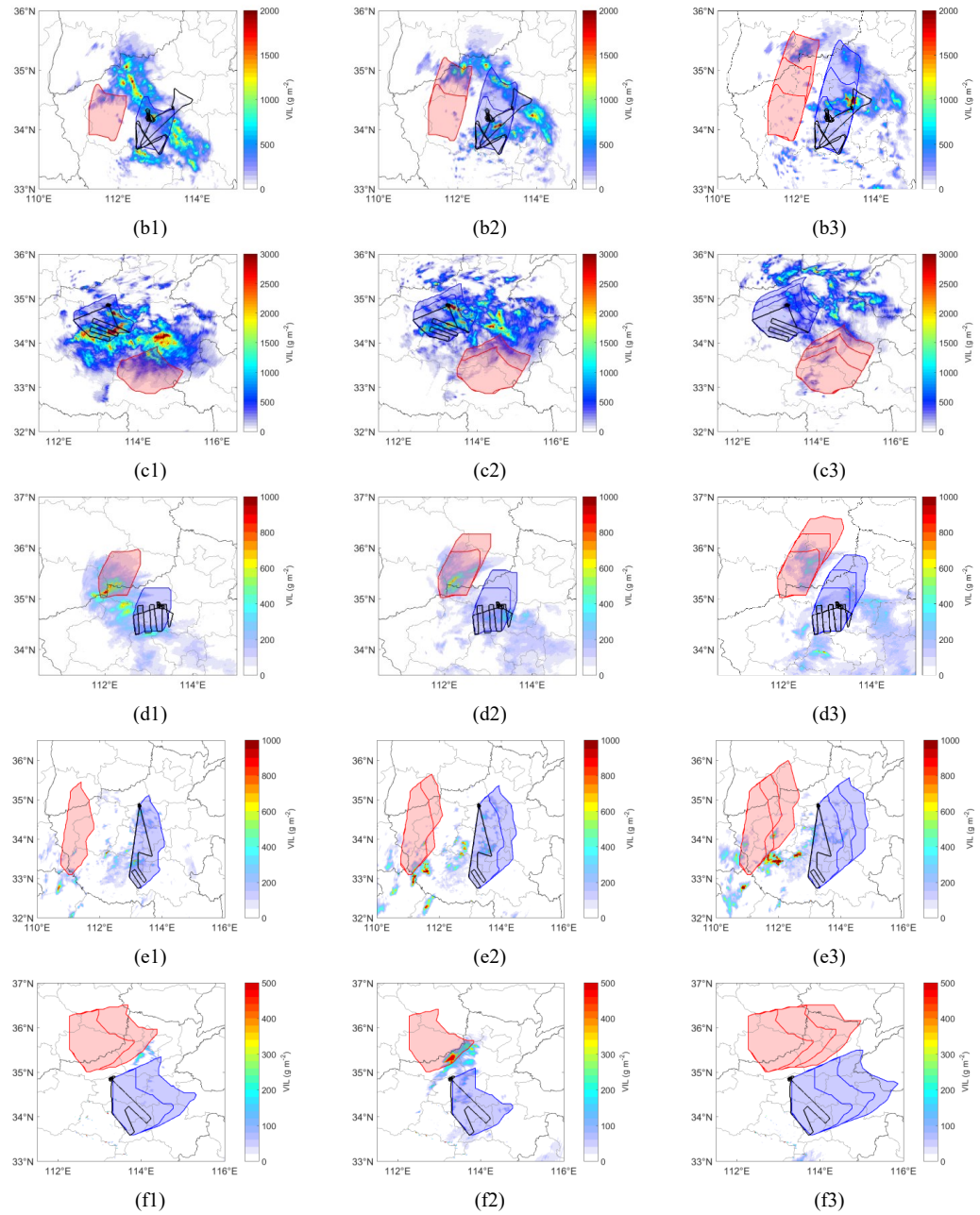


Figure 12: Same as Fig. 7, but for vertically integrated liquid water content.

Table 11. Area-averaged hourly vertically integrated liquid water content in the target and control areas after seeding operations.

Operation number	Time point (hour)	Area-averaged VIL in the target areas (g·m ⁻²)	Area-averaged VIL in the control areas (g·m ⁻²)
	1	307.81	381.65
1	2	296.92	313.76
	3	223.10	193.31
	1	324.59	98.05
2	2	275.99	124.93
	3	200.51	70.04



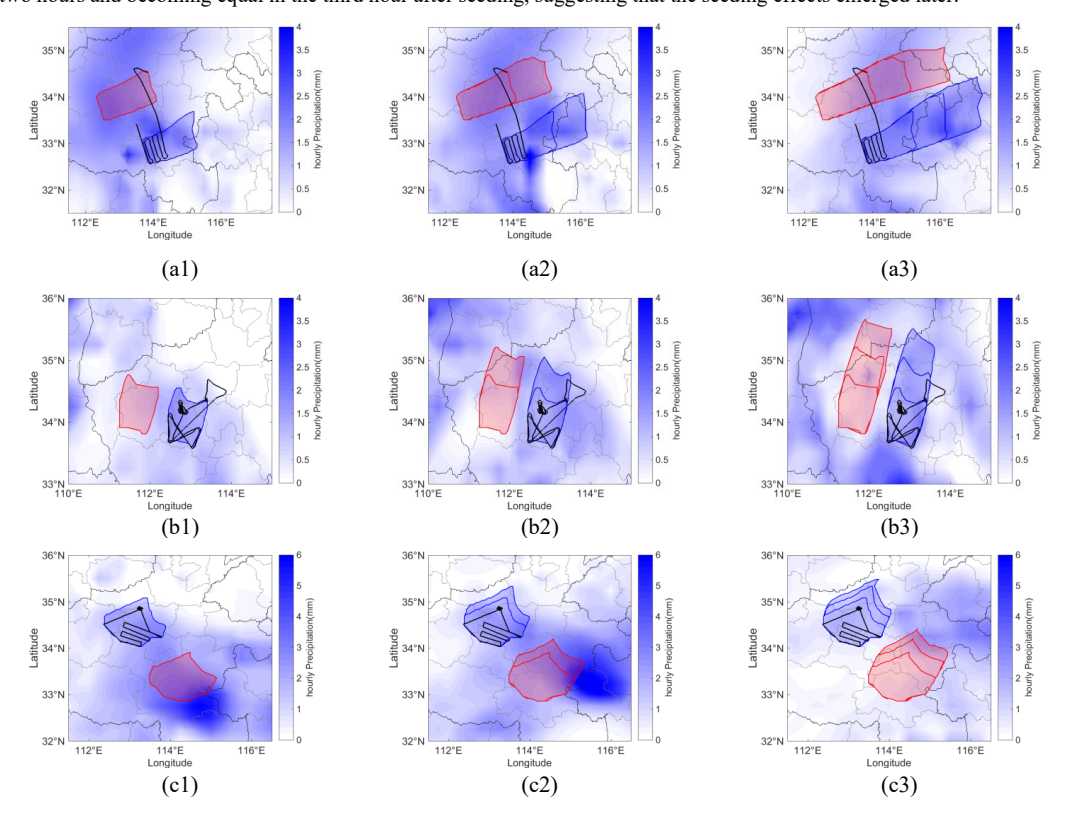
420



	1	603.01	468.46
3	2	695.27	262.37
	3	298.92	102.28
	1	68.75	163.25
4	2	68.16	141.13
	3	53.20	85.80
	1	46.39	6.08
5	2	42.00	15.02
	3	23.74	15.02
	1	13.09	56.87
6	2	5.73	13.55
	3	0.81	0.43

410 8. Analysis of hourly precipitation

Figure 13 and Table 12 present the changes in hourly precipitation in the target and control areas during 1–3 hours after cloud seeding and the area-averaged hourly precipitation. On this basis, the effects of cloud seeding on hourly precipitation were analyzed. Across the six operations, the mean value of hourly precipitation ranged from 0.0002 to 1.81 mm in the target areas, and ranged from 0 to 3.1 mm in the control areas. The maximum difference in hourly precipitation between the two areas reached 1.59 mm. The change rates of hourly precipitation induced by seeding varied considerably from 38.2% to 89.1% across different operations. Specifically, the highest change rates (> 80%) were observed in Operations No. 4 and No. 5, while the lowest (38.2%) was in Operation No. 6. In Operation No. 4, the change rate reached 89.1%, where the target areas recorded markedly higher precipitation than the control areas, particularly during the latter two hours. In Operation No. 5, the change rate was 87.1%, with precipitation in the target area remaining consistently lower than that in the control areas during the first two hours and becoming equal in the third hour after seeding, suggesting that the seeding effects emerged later.







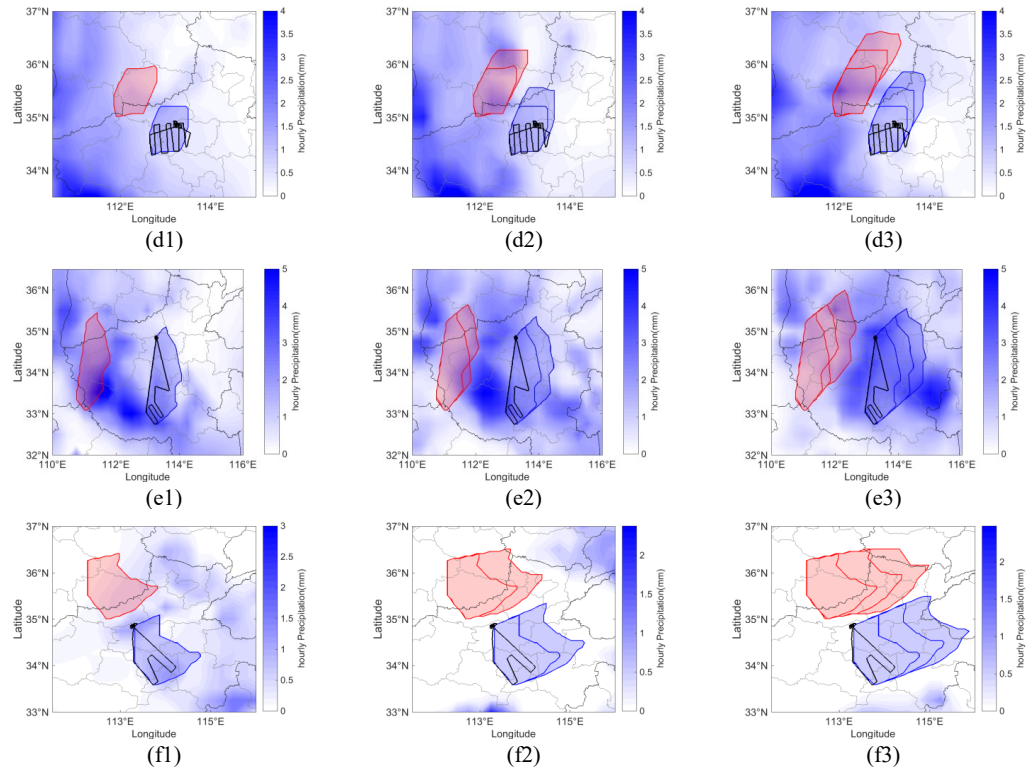


Figure 13: Same as Fig. 7, but for hourly precipitation amount.

Table 12. Area-averaged hourly precipitation and its change rates over the target and control areas after seeding operations.

	-		_	~ -
Operation number	Time point (hour)	Area-averaged hourly precipitation in the target areas (mm)	Area-averaged hourly precipitation in the control areas (mm)	Change rates of hourly precipitation
1	1	1.275	1.437	
	2	1.608	2.187	71.7%
	3	1.438	1.679	
2	1	0.899	0.419	
	2	0.983	0.874	69.5%
	3	0.885	0.417	
3	1	1.511	3.096	
	2	1.419	2.750	51.7%
	3	0.634	0.880	
4	1	0.465	0.466	
	2	0.489	1.271	89.1%
	3	0.491	1.259	
5	1	1.589	1.756	
	2	1.097	1.447	87.1%
	3	1.812	1.806	
6	1	0.3723	0.2592	
	2	0.0041	0.0127	38.2%
	3	0.0002	0.0000	

3.5.2 The change rates of multiple indicators induced by cloud seeding

Figures 14–16 present the change rates for each evaluation indicator and the integrated index PIDI for the six operations. The PIDI values for the seven indicators induced by seeding ranged from 15.0% to 69.7%, showing a smaller variation



435

445



magnitude compared with the change rates of individual indicators, which reflects the synergistic effects of multiple indicators. The change rates of hourly precipitation induced by seeding varied from 38.2% to 89.1%. Across six operations, Operation No. 4 exhibited the largest increase in hourly precipitation (89.1%), accompanied by a sharp decrease in cloud-top temperature (-91.4%), a surge in optical thickness (121.7%), and the maximum increase in liquid water path (79.3%), indicating ideal conditions for cold-cloud seeding. Operation No. 5 also presented an increase in hourly precipitation (87.1%) but decrease in composite reflectivity (-33.9%) and strong-echo area (-40.6%), suggesting enhanced precipitation efficiency rather than increased intensity. The change rates of cloud-top temperature ranged widely from -91.4% to 67.0%, showing the most pronounced bidirectional changes with one positive and four negative cases. The change rates of cloud effective radius were tightly clustered between 8.9% and 9.1%. The change rates of optical thickness spanned from -14.7% to 121.7%, with the exceptionally high value 121.7% in Operation No. 4 possibly reflecting the ice-water phase change within the cloud. The change rates of liquid water path in the two operations ranged from 4.2% to 79.3%. The change rates of radar reflectivity varied between -33.9% and 21.5%, with three positive and three negative cases. The strong-echo area increased in most operations, ranging from -40.6% to 28.2%, with five positive and one negative cases. The change rates of VIL varied between -36.0% and 19.4%, with four positive and two negative cases.

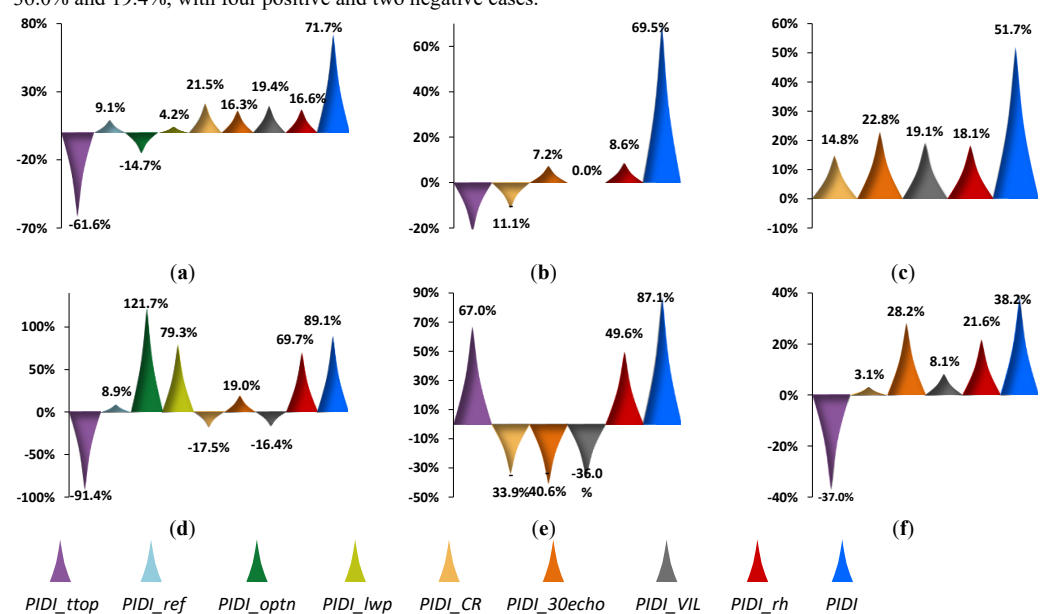


Figure 14: The change rates for each evaluation indicator and the integrated index of seven indicators (physical inspection dimensionless index; PIDI) for the six operations (a-f). PIDI_ttop, PIDI_ref, PIDI_optn, PIDI_lwp, PIDI_CR, PIDI_30echo, PIDI_VIL and PIDI_rh represent the change rates of cloud-top temperature, cloud effective radius, optical thickness, liquid water path, composite reflectivity, ≥ 30 dBZ echo area, VIL and hourly precipitation in the target areas caused by seeding, respectively. The PIDI represents the average change rate of the seven indicators induced by cloud seeding in the target areas.

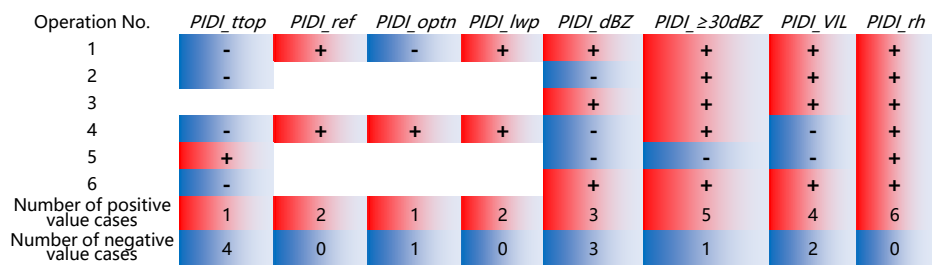


Figure 15: The distribution of positive and negative values of the change rates of each evaluation indicator for the six operations.





455

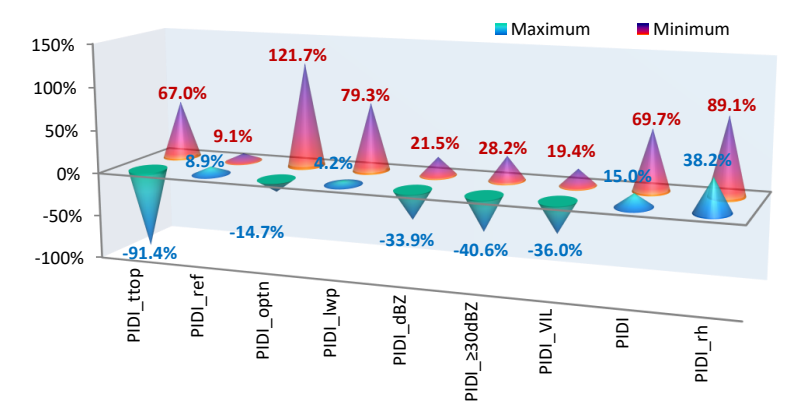


Figure 16: Maximum and minimum values of the change rates for each evaluation indicator and the integrated index PIDI for the six operations. Red and green cones represent the maximum and minimum values, respectively.

4. Discussion

460

465

470

475

The objectivity and accuracy of the physical evaluation of cloud seeding effects are constrained by multiple factors. This section discusses several key aspects that may influence the evaluation results.

In the process of identifying the control area, even when theoretically sound methods are employed, it is often difficult to find an ideal control area that is highly similar to the target area in nature. This challenge is particularly pronounced for cloud systems with highly strong turbulence, as no two entities possess identical physical properties. Consequently, the natural variabilities of clouds and precipitation cannot yet be fully eliminated from the evaluation results. To enhance the scientific rigor and accuracy of the evaluation results, it is advisable to select control areas from a case database encompassing extensive historical weather events and observational data, thereby facilitating the identification of control areas with higher similarity.

The selection of the evaluation time window may also affect the evaluation results. In this study, a three-hour period after the end time of seeding operations was adopted to represent the average duration of seeding effects. However, the aircraft-based operation performs a dynamic line-source seeding along the flight path, typically lasting from several minutes to several hours. Consequently, the onset of seeding effects differs across individual seeding points or segments along the flight line. From a more rigorous scientific perspective, conducting an evaluation that considers the spatio-temporal evolution of seeding effects for each operational segment may yield a more precise understanding of the process.

The entropy weight method has the limitation of being highly dependent on the sample data, with the weights varying as the samples change. Therefore, both the number and the features of seeding cases can exert a certain influence on the evaluation results.

Additionally, the HYSPLIT model introduces another source of uncertainty, as it treats seeding agents as passive tracers and neglects their nucleation interactions with cloud droplets or ice crystals. In reality, the ice-nucleating efficiency of AgI particles is strongly influenced by temperature, humidity and cloud microphysical conditions. For a more refined evaluation



490

495

500

505

510

515

520



480 of seeding effects, the HYSPLIT model could be coupled with cloud models such as WRF-CHEM. Further enhancements to its capability in simulating seeding agent dispersion could be achieved through tighter coupling with cloud microphysics and the incorporation of high-resolution turbulence parameterizations.

The reliability of cloud seeding effect evaluation is highly dependent on the quality of meteorological data. Both the spatio-temporal resolution of atmospheric fields and observational errors in cloud and precipitation measurements can influence the evaluation results. In this study, ERA5 reanalysis data with spatio-temporal resolutions of one hour and $0.25^{\circ}\times0.25^{\circ}$ were used. Using data with resolutions improved to several minutes and a few kilometers would yield more detailed and scientifically robust evaluation results. During the dimensionless processing of evaluation indicators, the standardization using the min-max normalization method depends solely on the maximum and minimum values of each indicator. This suggests that changes in weights depend heavily on these two extreme values, thereby requiring rigorous and precise quality control of the observational data.

5. Conclusions

This study developed a physical evaluation method for cloud seeding effects that integrates several key techniques to reduce the interference of natural precipitation variability, separate seeding-induced precipitation enhancement from natural precipitation, and achieve an integrated quantitative evaluation based on multiple indicators. Main conclusions are as follows:

- (1) The six operations exhibited nonlinear growth patterns for dispersion in both the target and control areas, with rapid expansion at the initial stage followed by a slower rate. The dispersion rate, distance, extent and concentration of the seeding agent vary significantly depending on the meteorological conditions.
- (2) The VIL showed notably high entropy weights (0.06–0.43) in multiple operations (No. 2, 3 and 6), making it a relatively stable indicator for evaluating the cloud seeding effects.
- (3) For the six operations, due to complex cloud microphysical processes such as latent heat release from deposition, downdrafts, cloud dissipation and cloud development, the responses of cloud-top temperature to seeding varied considerably $(-44.56^{\circ}\text{C}\sim-6^{\circ}\text{C})$.
- (4) The effects of cloud seeding on cloud effective radius and optical thickness are complex and vary substantially depending on specific seeding conditions. The responses of liquid water path were time-dependent, the seeding-induced responses of radar reflectivity exhibited distinct patterns, including delayed manifestation, strong enhancement, and ineffectiveness or being masked. The strong-echo area and the VIL in the target areas fluctuated and generally decreased over time, respectively.
- (5) The integrated PIDI values for the seven indicators ranged from 15.0% to 69.7%, showing a smaller variation magnitude compared with the change rates of individual indicators, which reflects the synergistic effects of multiple indicators.

Acknowledgements: Conceptualization, X.S., X.L. and R.C.; methodology, X.S., X.L. and J.D.; software, X.S., X.L. and B.C.; validation, Y.L., F.Z. and C.S.; data curation, Y.X., and S.W.; writing—original draft preparation, X.S. and X.L.; writing—review and editing, J.D. and R.C.; visualization, B.C.; supervision, Y.L.; project administration, F.Z.; funding acquisition, X.S. All authors have read and agreed to the published version of the manuscript.

Financial support: This research was funded by the Construction Project of Weather Modification Ability in the Central China: Research Experiment on Rain & Snow Enchancement Through Cloud Seeding in Stratiform Clouds with Embedded Convection in the Central China (Shangqiu) (grant number ZQC-H22256), the Project of Joint Fund for Science and Technology Research and Development of Henan Province (grant number 242103810091), the Project of WMC Key Innovation Team (grant number WMC2023IT03), the He'nan Key Laboratory of Agrometeorological Support and Applied Technique Research Project of China Meteorological Administration (grant number KM202327, KM202135). The APC was funded by the Project of Joint Fund for Science and Technology Research and Development of Henan Province (grant number 242103810091).



550

555

560



525 **Conflicts of Interest:** The authors declare no conflicts of interest.

References

- Crawford, I., Bower, K. N., Choularton, T. W., Dearden, C., Crosier, J., Westbrook, C., Capes, G., Coe, H., Connolly, P. J., Dorsey, J. R.: Ice formation and development in aged, wintertime cumulus over the UK: Observations and modelling, Atmos. Chem. Phys., 12, 4963-4985, https://doi.org/10.5194/acp-12-4963-2012, 2012.
- 530 Cui, K., Wang, H., Ke, Y., Dong, X., Yang, Y., Wu, Z., Liu, S., Wang, Z., Lin, W., Zhao, T.: In-situ aircraft observations of aerosol and cloud microphysical characteristics of mixed-phase clouds over the North China Plain, Science of the Total Environment 949, 175248, https://doi.org/10.1016/j.scitotenv.2024.175248, 2024.
 - Dong, X., Sun, X., Yan, F., Zhang, J., Wang, S., Peng, M., Zhu, H.: Aircraft Observation of a Two-Layer Cloud and the Analysis of Cold Cloud Seeding Effect, Frontiers in Environmental Science, 10, 855813, https://doi.org/10.3389/fenvs.2022.855813, 2022.
 - Dong, X., Zhao, C., Yang, Y., Wang, Y., Sun, Y., Fan, R.: Distinct change of supercooled liquid cloud properties by aerosols from an aircraft-based seeding experiment, Earth Space Sci., 7(8), e2020EA001196, https://doi.org/10.1029/2020EA001196, 2020.
- Flossmann, A. I., Manton, M., Abshaev, A., Bruinties, R., vurakami, M., Prabhakaran, T., Yao, Z.: Review of Advances in Precipitation Enhancement Research, Bull. Am. Meteorol. Soc., 100, 1465-1480, https://doi.org/10.1175/BAMS-D-18-0160.1, 2010
 - Geerts, B., Miao, Q., Yang, Y., Rasmussen, R., Breed, D.: An AirborneProfling Radar Study of the Impact of Glaciogenic Cloud Seeding on Snowfalfrom winter Orographic Clouds, J. Atmos. Sci., 67(10), 3286-3302, https://doi.org/10.1175/2010JAS3496.1, 2010.
- 545 Grawe, S., Jentzsch, C., Schaefer, J., Wex, H., Mertes, S., Stratmann, F.: Next-Generation Ice-Nucleating Particle Sampling on Board Aircraft: Characterization of the High-Volume Flow aERosol Particle Filter Sampler (HERA), Atmospheric Measurement Techniques, 16, 4551-4570, https://doi.org/10.5194/egusphere-2025-4336, 2023.
 - Guo, X., Lin, D., Wu, F.: Analysis of Precipitation Process and Operational Precipitation Enhancement in Panxi Region Based on Cloud Parameters Retrievals from China's Next-Generation Geostationary Meteorological Satellite FY–4A, Atmosphere 14(6), 922, https://doi.org/10.3390/atmos14060922, 2023.
 - Guo, X., Zheng, G., Jin, D.: A numerical comparison study of cloud seeding by silver iodide and liquid carbon dioxide, Atmos. Res., 79, 183-226., https://doi.org/10.1016/j.atmosres.2005.04.005, 2006.
 - Hua, S., Chen, B., He, H., Chen, Y., Liu, X. e., Yang, J.: Numerical Simulation of the Cloud Seeding Operation of a Convective Rainfall Event Occurred in Beijing, Atmospheric Research, 304, 107386, https://doi.org/10.1016/j.atmosres.2024.107386,
 - Jia, S., Yao, Z.: Case Study on the Convective Clouds Seeding Effects in Yangtze-Huahe Region, Meteorological Monthly, 42(2), 238-245, https://doi.org/10.7519/j.issn.1000-0526.2016.02.012, 2016.
 - Lance, S., Brock, C. A., Rogers, D., Gordon, J. A.: Water Droplet Calibration of the Cloud Droplet Probe (CDP) and In-Flight Performance inLiquid, Ice and Mixed-phase Clouds during ARCPAC, Atmos. Meas. Tech., 3(6), 1683-1706, https://doi.org/10.5194/amt-3-1683-2010, 2010.
 - Li, D., 2002. Weather Modification: Current Status and Prospects. China Meteorological Press, Beijing.

 Liu, R., Zhou, H., Li, D., Zeng, L., Xu, P.: Evaluation of Artificial Precipitation Enhancement Using UNET-GRU Algorithm for Rainfall Estimation, Water, 15(8), 1585, https://doi.org/10.3390/w15081585, 2023.
- Rauber, R. M., Geerts, B., Xue, L., French, J., Friedrich, K., Rasmussen, R. M., Tessendorf, S. A.: Wintertime orographic cloud seeding-a review, J. Appl. Meteorol. Climatol., 58(10), 2117-2140, https://doi.org/10.1175/JAMC-D-18-0341.1, 2019. Ren, J., Zhang, W., Kou, M., Ma, Y., Zhang, X.: A Numerical Study of Critical Variables on Artificial Cold Cloud Precipitation Enhancement in the Qilian Mountains, China, Atmosphere, 14(7), 1086, https://doi.org/10.3390/atmos14071086, 2023.
 - Sha, X., Chu, R., Li, M., Xiao, Y., Ding, J., Feng, L.: Transmission of Seeding Agent for Aircraft Precipitation Enhancement Based on the HYSPLIT Model, Atmosphere, 13(9), 1508, https://doi.org/10.3390/atmos13091508, 2022.





- 570 Silverman, B. A.: A critical assessment of glaciogenic seeding of convective clouds for rainfall enhancement, Bull. Am. Meteor. Soc., 82, 903-924, https://doi.org/10.1175/1520-0477(2001)082 < 903-323.co;2, 2001.
 - Wan, X., Zhou, S., Fan, Z.: Comprehensive Efficiency Evaluation of Aircraft Artificial Cloud Seeding in Hunan Province, China, Based on Numerical Simulation Catalytic Method, Atmosphere, 14(7), 1187, https://doi.org/10.3390/atmos14071187, 2023.
- Wang, F., Chen, B., Yue, Z., Wang, J., Li, D., Lin, D., Tang, Y.: A Composite Approach for Evaluating Operational Cloud Seeding Effect in Stratus Clouds, Hydrology, 11, 167, https://doi.org/10.3390/hydrology11100167, 2024.
 - Wang, F., Li, J., Yao, Z., Li, D., Li, J.: Advances of Quantitative Evaluation Studies of Artificial Precipitation Enhancement in China, Meteorological Monthly, 48(8), 945-962, https://doi.org/10.7519/j.issn.1000-0526.2022.012701, 2022.
- Wang, J., Yue, Z., Rosenfeld, D., Zhang, L., Zhu, Y., Dai, J.: The Evolution of an AgI Cloud-Seeding Track in Central China as Seen by a Combination of Radar, Satellite, and Disdrometer Observations, Geophys. Res. Atmos., 126(11), e2020JD033914, https://doi.org/10.1029/2020JD033914, 2021.
 - WMO, 2015. Documents on Weather Modification. In Proceedings of the Expert Team on Weather Modification Research, Phitsanulok Thailand.
- Wu, X., Niu, S., Fin, D., Sun, H.: Infuence of natural rainfall variability on the evaluation of artificial precipitation enhancement, Sci. China Earth Sci., 58, 906-914, https://doi.org/10.1007/s11430-015-5055-0, 2015.
 - Wu, X., Yan, N., Yu, H., Niu, S., Meng, F., Liu, W., Sun, H.: Advances in the Evaluation of Cloud Seeding: Statistical Evidence for the Enhancement of Precipitation, Earth and Space Science 5, 425-439, https://doi.org/10.1029/2018EA000424, 2018.
- Xue, L., Tessendorf, S. A., Nelson, E., Rasmussen, R. M., Breed, D., Parkinson, S., Holbrook, P., Blestrud, D.: Implementation of asilver iodide cloud-seeding parameterization in WRF. Part II: 3D simulations of actual seeding events and sensitivity tests, J. Appl. Meteorol. Climatol., 52, 1458-1476, https://doi.org/10.1175/JAMC-D-12-0149.1, 2013.
 - Yan, L., Zhou, Y., Wu, Y., Cai, M., Peng, C., Song, C., Liu, S., Liu, Y.: FY-4A Measurement of Cloud-Seeding Effect and Validation of a Catalyst T&D Algorithm, Atmosphere, 15(5), 556, https://doi.org/10.3390/atmos15050556, 2024.
- Yang, W. X., Fang, B., Zhang, J. N., Cui, Y., Hou, S. Y.: Warm Cloud Seeding Experiment of Aircraft Precipitation

 595 Enhancement for the Northward Typhoon In-Fa in China, Applied Ecology and Environmental Research, 21(5), 3887–3894,

 https://doi.org/10.15666/aeer/2105_38873894, 2023.
 - Yoo, C., Na, W., Cho, E., Chang, K.-H., Yum, S. S., Jung, W.: Evaluation of Cloud Seeding on the Securement of Additional Water Resources in the Borycong Dam Basin, Korea, Journal of Hydrology, 613, 128480, https://doi.org/10.1016/j.jhydrol.2022.128480, 2022.
- Yu, X., Wang, X. L., Dai, J.: Research on simulation of effective range for cloud seeding by aircraft within super-clooled stratus, Acta Meteorol. Sin., 60, 205-214, https://doi.org/10.11676/gxxb2002.025, 2002.
 - Zhang, R., Liu, L., Zhong, X., Gao, A.: Evaluation of Aircraft Weather Modification in Guangxi by the Use of CINRAD Observations, Meteorological Monthly, 36(2), 70-75, https://doi.org/10.3788/HPLPB20102207.1462, 2010.
- Zhang, Y., Kang, X., Hou, Y., Xue, L., Tian, J.: Application of machine learning algorithm in the effect verification of artificial rainfall on the upper reaches of the Yellow River, Journal of the Meteorological Sciences, 44(6), 1154-1162, https://doi.org/10.12306/2021jms.0098 2024.
 - Zheng, H., Zhang, Y., Chen, Y., Ding, D., Wu, Z., Huang, M., He, H.: Microphysical and Dynamic Evolution of Convection Observed by Polarimetric Radar under the Influence of Cloud Seeding, Atmospheric Research, 297, 107110, https://doi.org/10.1016/j.atmosres.2023.107110, 2024.